

Elemental abundance pattern and temperature inversion on the dayside of HAT-P-70b observed with CARMENES and PEPSI

B. Guo^{1,2}, F. Yan¹, Th. Henning³, L. Nortmann², M. Stangret⁴, D. Cont^{5,6}, E. Pallé^{7,8}, D. Shulyak⁹, K. G. Strassmeier^{10,11}, I. Ilyin¹⁰, F. Lesjak^{2,10}, A. Reiners², S. Liu¹, K. Molaverdikhani^{5,6}, G. Scandariato¹², E. Keles¹³, J. A. Caballero¹⁴, P. J. Amado⁹, A. Quirrenbach¹⁵, I. Ribas^{16,17}, S. Góngora¹⁸, A. P. Hatzes¹⁹, M. López-Puertas⁹, D. Montes²⁰, K. Poppenhaeger^{10,11}, E. Schlawin²¹, A. Schweitzer²², and D. Sicilia¹²

¹ Department of Astronomy, University of Science and Technology of China, Hefei 230026, China
e-mail: yanfei@ustc.edu.cn

² Institut für Astrophysik und Geophysik, Georg-August-Universität, Friedrich-Hund-Platz 1, 37077 Göttingen, Germany

³ Max-Planck-Institut für Astronomie, Königstuhl 17, 69117 Heidelberg, Germany

⁴ INAF – Osservatorio Astronomico di Padova, Vicolo dell’Osservatorio 5, 35122, Padova, Italy

⁵ Universitäts-Sternwarte, Ludwig-Maximilians-Universität München, Scheinerstrasse 1, 81679 München, Germany

⁶ Exzellenzcluster Origins, Boltzmannstrasse 2, 85748 Garching bei München, Germany

⁷ Instituto de Astrofísica de Canarias, 38205 La Laguna, Tenerife, Spain

⁸ Departamento de Astrofísica, Universidad de La Laguna, 38206 La Laguna, Tenerife, Spain

⁹ Instituto de Astrofísica de Andalucía (IAA-CSIC), Glorieta de la Astronomía s/n, 18008 Granada, Spain

¹⁰ Leibniz-Institut für Astrophysik Potsdam, An der Sternwarte 16, 14482 Potsdam, Germany

¹¹ Universität Potsdam, Institut für Physik und Astronomie, Karl-Liebknecht-Str. 24/25, 14476 Potsdam-Golm, Germany

¹² INAF – Osservatorio Astrofisico di Catania, Via S. Sofia 78, 95123 Catania, Italy

¹³ Freie Universität Berlin, Institute of Geological Sciences, Malteserstrasse 74-100, 12249 Berlin, Germany

¹⁴ Centro de Astrobiología (CSIC-INTA), Camino Bajo del Castillo s/n, Campus ESAC, 28692 Villanueva de la Cañada, Madrid, Spain

¹⁵ Landessternwarte, Zentrum für Astronomie der Universität Heidelberg, Königstuhl 12, 69117 Heidelberg, Germany

¹⁶ Institut de Ciències de l’Espai (CSIC), c/ de Can Magrans s/n, Campus UAB, 08193 Bellaterra, Barcelona, Spain

¹⁷ Institut d’Estudis Espacials de Catalunya, 08860 Castelldefels, Barcelona, Spain

¹⁸ Departamento de Física de la Tierra y Astrofísica & IPARCOS Instituto de Física de Partículas y del Cosmos, Facultad de Ciencias Físicas, Universidad Complutense de Madrid, Plaza de Ciencias 1, 28400 Madrid, Spain

¹⁹ Thüringer Landessternwarte Tautenburg, Sternwarte 5, 07778 Tautenburg, Germany

²⁰ Centro Astronómico Hispano en Andalucía, Observatorio Astronómico de Calar Alto, Sierra de los Filabres, 04550 Gérgal, Almería, Spain

²¹ Steward Observatory, University of Arizona, 933 N. Cherry Ave., Tucson, AZ 85721, USA

²² Hamburger Sternwarte, Gojenbergsweg 112, 21029 Hamburg, Germany

Received 30 October 2025 / Accepted 14 December 2025

ABSTRACT

Ground-based high-resolution spectroscopic observations have identified various chemical species in the atmosphere of numerous ultra-hot Jupiters (UHJs), including neutral and ionized metals. These detections have offered valuable insights into planet formation mechanisms via abundance measurements of refractory elements. We observed the dayside thermal emission spectrum of UHJ HAT-P-70b using the high-resolution spectrographs CARMENES and PEPSI. Through our cross-correlation analysis, we detected emission signals for Al I, Al II, Ca II, Cr I, Fe I, Fe II, Mg I, Mn I, and Ti I, marking the first detection of Al I and Al II in an exoplanetary atmosphere. Tentative signals of C I, Ca I, Na I, Na II, and Ni I were also identified. Based on those detections, we were able to perform atmospheric retrievals to constrain the thermal profile and elemental abundances of the planet’s dayside hemisphere. The retrieved temperature–pressure profile reveals a strong temperature inversion layer. The chemical free retrieval yielded a metallicity of $[\text{Fe}/\text{H}] = 0.38^{+0.74}_{-1.11}$, while the chemical equilibrium retrieval resulted in $[\text{Fe}/\text{H}] = 0.23^{+1.08}_{-0.98}$, with both values consistent with the solar metallicity. We also tentatively found an enriched abundance of Ni, which could result from the accretion of Ni-rich planetesimals during the planet’s formation. On the other hand, elements with condensation temperatures above 1400 K (e.g., Ca, Ti, and V) appear to be slightly depleted, possibly due to cold-trapping on the planet’s nightside. However, Al, with the highest condensation temperature at 1653 K, displays a solar-like abundance, which might reflect the formation-related enrichment of Al. Our retrieval indicates extremely high volume mixing ratios of metal ions (Fe II and Ca II), which are significantly inconsistent with predictions from chemical equilibrium models. This disequilibrium suggests that the atmosphere is likely undergoing significant hydrodynamic escaping, which enhances the atmospheric density at high altitudes where the ionic lines are formed.

Key words. planets and satellites: atmosphere – techniques: spectroscopic – planets and satellites: individuals: HAT-P-70b

1. Introduction

Ultra-hot Jupiters (UHJs) represent a class of short-period gas giants that suffer extreme irradiation from the host star, typically resulting in high equilibrium temperatures ($T_{\text{eq}} > 2000$ K). In these extreme environments, the dayside hemisphere becomes dominated by atomic and ionic species as most molecules undergo thermal dissociation (e.g., Lothringer et al. 2018; Kitzmann et al. 2018; Parmentier et al. 2018). The combination of the expanded radius and strong spectral features makes UHJs optimal laboratories for detailed atmospheric characterization. Furthermore, radiative absorption by specific chemical constituents, such as iron, hydrogen, TiO, and VO (e.g., Fortney et al. 2008; Lothringer et al. 2018; García Muñoz & Schneider 2019; Fossati et al. 2021), creates temperature inversion layers where atmospheric temperature increases with altitude. This atmospheric phenomenon has been observationally confirmed in several UHJs, such as KELT-9b, KELT-20b, WASP-178b, and TOI-2109b (e.g., Pino et al. 2020; Yan et al. 2022b; Cont et al. 2024, 2025).

Recent advances in high-resolution spectroscopy have enabled unprecedented atmospheric characterization of UHJs, with both transmission and thermal emission spectra yielding critical insights. Ground-based high-resolution optical spectrographs, such as High Dispersion Spectrograph (HDS), Calar Alto high-Resolution search for M dwarfs with Exoearths with Near-infrared and optical Échelle Spectrographs (CARMENES), High Accuracy Radial velocity Planet Searcher for the Northern hemisphere (HARPS-N), and Echelle SpectroPolarimetric Device for the Observation of Stars (ESPaDOs), have resolved prominent Fe I signals in UHJs such as WASP-33b (e.g., Nugroho et al. 2020; Cont et al. 2021; Herman et al. 2022), alongside comprehensive detections of neutral and ionized metals (e.g., V I, Ti II, Ca II; Yan et al. 2019; Cont et al. 2022; Yang et al. 2024a). These findings are complemented by near-infrared (NIR) observations that have simultaneously revealed molecular constituents (e.g., CO, H₂O, OH; Nugroho et al. 2021; Yan et al. 2022a; Choi et al. 2025), providing multiwavelength constraints on atmospheric chemistry. Notably, NIR observations have also provided evidence of nightside emission (Yang et al. 2024b; Mraz et al. 2024). Additionally, Evans-Soma et al. (2025) also presented the detection of CH₄ in the nightside of WASP-121b with low-resolution JWST (James Webb Space Telescope) spectroscopic observations.

Bayesian spectral retrieval techniques now enable precise constraints on the atmospheric abundances of detected species. Notable findings include titanium depletion in WASP-76b observed via MAROON-X transmission spectra (Pelletier et al. 2023) attributed to nightside cold-trapping, a phenomenon that has also been identified in WASP-121b (Hoeijmakers et al. 2024). In contrast, detections of Ti I and TiO in hotter UHJs such as WASP-33b, WASP-189b, and MASCARA-1b (Cont et al. 2022; Prinoth et al. 2022; Scandariato et al. 2023; Guo et al. 2024) suggest that this condensation mechanism is suppressed at extremely high temperatures.

In addition, studies of carbon and oxygen abundances primarily focus on constraining the C/O ratio as a tracer of planet formation pathways (e.g., Öberg et al. 2011; Madhusudhan 2012; Madhusudhan et al. 2014, 2017; Cridland et al. 2019, 2020). For instance, a near-solar or elevated C/O ratio in WASP-76b (Weiner Mansfield et al. 2024) implies formation outer the CO snow line via gas accretion or between the soot line and the H₂O snow line. Conversely, the lower C/O ratio and solar to super-solar metallicity of KELT-20b (Finnerty et al. 2025) are

consistent with planet formation beyond the CO snow line, followed by Type II migration (Khorshid et al. 2022). Nevertheless, current elemental abundance measurements remain ambiguous, unable to definitively determine whether the lower C/O results from oxygen enrichment or carbon depletion. Intrinsic degeneracies persist in linking these ratios to specific protoplanetary disk regions, reflecting the complex interplay of gas and solid-phase accretion processes.

To break the inherent degeneracies in interpreting formation pathways using the C/O ratio alone, complementary measurements of other elemental tracers are required. The abundance of refractory elements (e.g., Si, Fe) in the atmosphere provides unique constraints on planetary formation histories (Lothringer et al. 2021). Although atmospheric condensation below 2000 K increases the probability to obscure refractory elemental signatures in cooler planets, the extreme thermal environments of UHJs preserve these diagnostic tracers. Chachan et al. (2023) demonstrated that combined refractory and volatile abundance analyses can pinpoint formation locations. For WASP-121b, using the high-resolution spectrograph IGRINS, Smith et al. (2024) suggested that the most likely formation was between the soot line and H₂O snow line, although formation scenarios between the H₂O and CO snow lines or beyond the CO snow line remain plausible. Additionally, high-resolution observations with CRIRES+ and ESPRESSO have revealed a volatile-to-refractory enrichment in the atmosphere of WASP-121b, supporting formation in the outer disk near the CO snow line, followed by inward migration (Pelletier et al. 2025).

In this study, we report the detection of multiple chemical species (e.g., Al I, Al H, Fe I, and Ti I) in the dayside hemisphere of the UHJ HAT-P-70b through high-resolution thermal emission spectroscopy. Using Bayesian atmospheric retrieval methods, we constrain key atmospheric properties, including temperature-pressure profiles and metallicity. Identified by Zhou et al. (2019), the gas giant planet revolves around an A-type host star with a period of 2.74 days and exhibits a strongly misaligned orbit (obliquity $\lambda = 107.9^{+2.0}_{-1.7}$ degrees; Bello-Arufe et al. 2022). Previous transmission spectroscopy with HARPS-N (Bello-Arufe et al. 2022) revealed atmospheric absorption features from hydrogen Balmer lines, ionized metals (Ca II, Cr II, Fe II), and neutral species (Cr I, Fe I, Mg I, Na I, V I), with tentative detections of Ca I and Ti II. Langeveld et al. (2025) also identified the Ca II triplet lines in the transmission spectra with GHOST. Our work presents the first thermal emission characterization of this exoplanet's dayside hemisphere.

This paper is structured as follows. The observational methodology and data reduction are presented in Sect. 2. The detection techniques for atmospheric composition, along with their corresponding results are detailed in Sect. 3. We describe the atmospheric retrieval framework and discuss the retrieval results in Sect. 4. The conclusions of our work are presented in Sect. 5.

2. Observations and data reduction

We observed the thermal emission spectra of HAT-P-70b's dayside hemisphere on November 23, 2020 (program ID: H20-3.5-015) and December 23, 2023 (as part of the CARMENES Legacy program), with the CARMENES high-resolution spectrograph (Quirrenbach et al. 2016) installed at the 3.5m telescope of the Observatorio Astronómico de Calar Alto in Almería, Spain. Both visible (VIS, 5200–9600 Å, $R \sim 94\,600$) and NIR (9600–17 100 Å, $R \sim 80\,400$) wavelength channels were used to observe the target simultaneously. In addition, thermal emission spectra of the UHJ were also observed during

the two nights of November 20, 2021 and December 9, 2021, with the Potsdam Echelle Polarimetric and Spectroscopic Instrument (PEPSI, [Strassmeier et al. 2015, 2018b](#)) mounted on the Large Binocular Telescope (LBT) at the Mount Graham International Observatory in Arizona, USA. These two nights covered similar planetary orbital to those observed with CARMENES, corresponding to before and after eclipse, respectively. During each observation night, we used the LBT in binocular mode, utilizing the cross-disperser (CD) of the PEPSI spectrograph with CD3 in the blue arm (4760–5430 Å, $R \sim 50\,000$) and CD6 in the red arm (7360–8900 Å, $R \sim 50\,000$). These observations were carried out as part of the PEPSI exoplanet transit survey (PETS), and this work is the sixth publication of the PETS series ([Keles et al. 2022](#); [Johnson et al. 2023](#); [Scandariato et al. 2023](#); [Petz et al. 2024](#); [Keles et al. 2024](#)). The detailed observation logs are presented in Table 1.

The raw CARMENES data were reduced using the CARACAL pipeline ([Zechmeister et al. 2014](#); [Caballero et al. 2016](#)), which performs standard calibration including dark subtraction, flat-field correction, wavelength calibration, and spectrum extraction. The pipeline produced two-dimensional (2D) spectra containing 61 spectral orders in the VIS channel and 28 orders in the NIR channel. Additionally, the noise estimates for each spectral data point were also directly obtained from the pipeline. The reduction of PEPSI data was performed on the Spectroscopic Data Systems ([Ilyin 2000](#); [Strassmeier et al. 2018a](#)), a generic software platform capable of fully processing PEPSI data from raw input to final output automatically without human intervention. The reduction process primarily included bias subtraction, flat-field correction, scattered light removal, wavelength calibration, and spectrum normalization. Ultimately, for the PEPSI data, we obtained order-merged spectra.

Initially, the original spectra were cleaned by masking the wavelength points with low signal-to-noise ratio (S/N). For the CARMENES data, a uniform S/N threshold of 30 was applied across all observations. For the PEPSI observations, the thresholds varied between nights and spectral arms: on the first night, we applied S/N cuts of 200 for the blue arm and 175 for the red arm, while on the second night a uniform threshold of 130 was used for both arms. In addition, for the red part of the PEPSI spectra, we also excluded wavelength regions affected by telluric O₂ absorption lines (7590–7700 Å, 8100–8370 Å). The masked data points accounted for approximately 30% of the total number of pixels. We then normalized the spectra using a seventh-order polynomial fit and applied a 5σ clipping to remove potential outliers, such as strong sky emission lines. For the CARMENES spectra, all spectral orders were further combined to produce one-dimensional (1D) spectra.

To eliminate the contributions of telluric and stellar lines, we applied the SYSREM algorithm ([Tamuz et al. 2005](#)) to correct for systematic effects. This principal component analysis approach requires no prior assumptions, operating directly on the observed spectral matrix and corresponding noise estimates. The algorithm iteratively optimizes temporal and spectral correction vectors to construct the SYSREM model, which captures time- and wavelength-dependent systematics. We performed ten iterations of this process on the normalized spectra, progressively refining systematic effect removal. The final corrected spectra were obtained by dividing the normalized spectra by the SYSREM model, yielding residual spectra ultimately used for cross-correlation analysis. Noise was calculated throughout the procedure using standard error propagation techniques. A detailed mathematical

description of the SYSREM algorithm can be found in [Czesla et al. \(2024\)](#).

3. Atmospheric composition detection

3.1. Detection methods

3.1.1. Model spectra

Prior to conducting cross-correlation analysis, we generated thermal emission spectral models for each chemical species in the atmosphere of HAT-P-70b. The model spectra were calculated in a manner similar to that described by [Yan et al. \(2020\)](#), employing a two-point temperature-pressure (T - P) profile with the higher altitude point (T_1, P_1) set at $T_1 = 4500$ K, $P_1 = 10^{-4}$ bar, and the lower altitude point (T_2, P_2) set at $T_2 = 2500$ K, $P_2 = 10^{-2}$ bar. The mixing ratio of each chemical species was assumed to be constant throughout the entire T - P profile and set to the solar abundance value. A full list of the investigated chemical species, as well as the opacity databases used, is provided in Table A.1. All parameters used in model calculation are summarized in Table 2. Since the mass of HAT-P-70b has not been precisely determined, with only an upper limit $M_p < 6.78 M_{\text{Jup}}$ reported by [Zhou et al. \(2019\)](#), and given prior detections of atmospheric signatures via planetary transmission spectra, we adopted a surface gravity of $\log g = 3.0$ (cgs) during model spectra calculation and following atmospheric retrievals. This choice was motivated by the requirement for a relatively low surface gravity, which would result in a larger atmospheric scale height, thereby producing strong atmospheric signals detectable by transmission spectroscopy.

We computed the planetary thermal emission spectra using the radiative transfer code `petitRADTRANS` ([Mollière et al. 2019](#)). To ensure consistency with the data reduction processing, we normalized the model spectra by dividing them with the black body radiation spectra of the host star, calculated at its effective temperature. The normalized spectra were then convolved with a Gaussian instrumental profile matching the resolution of the observing instrument, using the `broadGaussFast` code from `PyAstronomy` ([Czesla et al. 2019](#)). The final model spectra for several chemical species we used in the cross-correlation analysis are presented in Figs. 2, 3, and 7.

3.1.2. Accounting for SYSREM effects

During the data reduction process, we employed the SYSREM algorithm to eliminate the telluric and stellar lines (Sect. 2). This procedure can potentially affect the strength and shape of the planetary spectral lines in the data. Accounting for this effect by applying the identical SYSREM processing to the spectral model is expected to improve the detection capability of the cross-correlation method. Our results demonstrate (compared to the conventional approach that does not account for line distortions by SYSREM) that this method enhances the detection significance of the Fe I signal by approximately 1σ . The improvement was particularly pronounced for the higher resolution CARMENES observations.

Given the phase-dependent distortion of line profiles, we initially Doppler-shifted the model spectra into the planetary rest frame with the theoretical radial velocity (RV) at each orbital phase, yielding a phase-resolved 2D model spectral matrix in

Table 1: Observation logs.

	Date	Airmass change	Exposure time (s)	N_{spectra}	Phase coverage	S/N range ^(a)
CARMENES						
Night 1	2020-11-23	1.18–1.12–1.55	400	34	0.527–0.592	74–87
Night 2	2023-12-23	1.31–1.12–1.23	400	31	0.419–0.479	50–71
PEPSI						
Night 1	2021-11-20	1.28–1.08–1.19	300	45	0.530–0.590	209–233
Night 2	2021-12-09	1.60–1.08–1.10	300	45	0.418–0.478	134–175

Notes. ^(a) The S/N per pixel was measured at $\sim 6245 \text{ \AA}$ for CARMENES data and $\sim 5061 \text{ \AA}$ for PEPSI data.

Table 2: Parameters of the HAT-P-70 system.

Parameter (Unit)	Value ^(a)
<i>The star</i>	
Radius R_{\star} (R_{\odot})	$1.858^{+0.119}_{-0.091}$
Mass M_{\star} (M_{\odot})	$1.890^{+0.010}_{-0.013}$
Magnitude V (mag)	9.470 ± 0.004
Effective temperature T_{eff} (K)	8450^{+540}_{-690}
Systemic velocity v_{sys} (km s^{-1})	25.26 ± 0.11
Rotational velocity $v \sin i_{\star}$ (km s^{-1})	$99.85^{+0.64}_{-0.61}$
Metallicity [Fe/H]	$-0.059^{+0.075}_{-0.088}$
<i>The planet</i>	
Radius R_{p} (R_{Jup})	$1.87^{+0.15}_{-0.10}$
Mass M_{p} (M_{Jup})	< 6.78 (3σ)
Surface gravity $\log g$ (log cgs)	< 3.73 (3σ)
Equilibrium temperature T_{eq} (K) ^(b)	2562^{+43}_{-52}
Inclination i_{p} (deg)	$96.50^{+1.42}_{-0.91}$
Orbital period P (d)	$2.74432452^{+0.00000079}_{-0.00000068}$
Transit epoch T_0 (BJD–TDB)	$2458439.57519^{+0.00045}_{-0.00037}$
Transit duration T_{14} (h)	$3.480^{+0.067}_{-0.048}$
RV semi-amplitude K_{p} (km s^{-1})	$186.82^{+0.33}_{-0.43}$

Notes. ^(a) All parameters except K_{p} , which was calculated by Eq. (2), were adopted from Zhou et al. (2019). ^(b) T_{eq} calculated assuming 0 Bond albedo and full heat redistribution.

the planetary rest frame:

$$v_{\text{p}} = v_{\text{sys}} - v_{\text{bary}} + K_{\text{p}} \sin 2\pi\phi, \quad (1)$$

$$K_{\text{p}} = \left(\frac{2\pi G M_{\star}}{P} \right)^{\frac{1}{3}} \sin i_{\text{p}}, \quad (2)$$

where v_{sys} is the systematic velocity, v_{bary} is the barycentric velocity of the observer on the Earth, ϕ is the planetary orbital phase ($\phi = 0$ corresponds to the middle transit time), G is the gravitational constant, P is the orbital period, M_{\star} is the stellar mass, and i_{p} is the orbital inclination, with all adopted parameter values summarized in Table 2. We utilized the accelerated SYSREM framework described by Gibson et al. (2022) to optimize computational efficiency. Following this approach, during the application of SYSREM to the observed spectra, a corresponding filter matrix was simultaneously generated. The filter was then applied to the model spectral matrix, resulting in a SYSREM-processed model spectral matrix. A model spectral grid was then generated by Doppler-shifting the model

across RV from -250 km s^{-1} to 250 km s^{-1} in 1 km s^{-1} increments, which were ready for the final cross-correlation analysis.

3.1.3. Cross-correlation

The cross-correlation function (CCF) was computed as the sum of the products of the model and residual spectra, weighted at each wavelength point by the inverse square of the observational noise ($1/\sigma^2$). For a given orbital phase, ϕ , and velocity shift, v , the CCF was calculated as

$$\text{CCF}(v, \phi) = \sum_{N_{\lambda}} \frac{r(\phi, \lambda) m(v, \phi, \lambda)}{\sigma(\phi, \lambda)^2}, \quad (3)$$

where $r(\phi, \lambda)$ and $\sigma(\phi, \lambda)$ represent the residual spectra and their corresponding noise, respectively, $m(v, \phi, \lambda)$ denotes the model spectra, and the summation was performed over all N_{λ} wavelength points.

The PEPSI spectra were contaminated by scattered moonlight during the first night, when the Moon-target angular separation was only about 14 deg and the observation occurred close to the full moon. To mitigate this effect, we excluded CCF within the RV range of $-15 < \text{RV} < 15 \text{ km s}^{-1}$ in the observer’s rest frame, as the moonlight contamination contains reflected sunlight whose spectral lines are nearly consistent with the observer’s frame. Figure 1 shows the resulting CCF map for Fe I obtained from PEPSI data. Although SYSREM processing suppressed much of this contamination, making it not visually prominent in the final CCF map, we found that excluding this RV range still marginally increased the detection significance compared to the unmasked case. Therefore, this masking procedure was retained. In contrast, the CARMENES observations remained unaffected by lunar contamination and therefore required no additional processing.

The CCFs were initially calculated in the observer’s rest frame. To search for the planetary atmosphere signal, we transformed the CCFs into the planetary rest frame using Eq. (1), by applying a range of trial values for K_{p} , ranging from 100 to 300 km s^{-1} in 1 km s^{-1} increments. For each trial K_{p} , the CCFs were integrated along the orbital phase axis to yield a 1D array. The horizontal axis of this array corresponds to the RV relative to the planetary rest frame ($\text{RV} = 0$), which we denote as Δv . The parameter Δv quantifies the uncertainty of v_{sys} , while also provides critical insights into planetary rotation and atmospheric circulation patterns. The ensemble of 1D arrays from all K_{p} trials was stacked to form a 2D parameter map ($K_{\text{p}}-\Delta v$ map). To evaluate the detection significance, we constructed the S/N map by normalizing a $K_{\text{p}}-\Delta v$ map for each species with the standard deviation of the noise-dominated regions ($50 \text{ km s}^{-1} < |\Delta v| < 100 \text{ km s}^{-1}$ and $100 \text{ km s}^{-1} < K_{\text{p}} < 300 \text{ km s}^{-1}$), excluding the

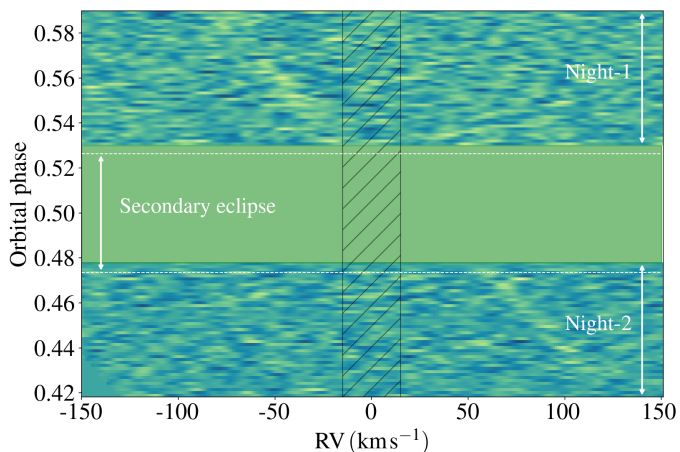


Fig. 1: CCF for Fe I in the observer’s rest frame, obtained from PEPSI observations. Horizontal dashed lines indicate the temporal boundaries of the secondary eclipse. The hatched region highlights the moonlight-contaminated zone, which was systematically masked during the construction of the K_p – Δv map.

central signal peak. A significant signal near the theoretical K_p and $\Delta v = 0$ in the S/N map provides conclusive evidence of the presence of the chemical species in the planetary atmosphere.

3.2. Detection results

We detected the atmospheric emission signals of Al I, AlH, Ca II, Cr I, Fe I, Fe II, Mg I, Mn I, and Ti I. The corresponding S/N maps are illustrated in Figs. 2 and 3, which combine all observations from CARMENES and PEPSI. We combined the K_p – Δv maps from all observations and subsequently normalized the result to obtain the final S/N map. This procedure effectively corresponds to a weighted summation, with the final map being predominantly dominated by the PEPSI observations with higher S/N. For each species, we selected the SYSREM iteration that yields the highest significance value in the S/N map. Figure A.1 illustrates the variation of the Fe I signal S/N with the number of SYSREM iterations. Other species exhibit a similar behavior, with their S/N values converging after approximately two iterations. A summary of the detection results is provided in Table 3.

This work presents the first thermal emission observation of HAT-P-70b, and reports the first detection of Al I, AlH, Mn I, and Ti I in its atmosphere. The detections of Ca II, Cr I, Fe I, Fe II, and Mg I are consistent with previous transmission spectroscopy results from HARPS-N (Bello-Arufe et al. 2022). To further validate the Ca II signal, we inspected its individual triplet lines in the residual spectra (Fig. 4). We detected the first and third lines of the Ca II triplet, which independently confirms the detection of Ca II previously reported from GHOST transmission observations (Langeveld et al. 2025).

General velocity offsets are observed among the detected signals. The K_p values for Al I, AlH, Ca II, and Fe I cluster around 190 km s^{-1} , closely matching the theoretically expected value of $186.82^{+0.33}_{-0.43} \text{ km s}^{-1}$. Conversely, Cr I, Mn I, and Ti I yield K_p near 200 km s^{-1} , whereas Fe II and Mg I are detected around 180 km s^{-1} . Despite these variations, the large measurement uncertainties of 6–35 km s^{-1} render all observed K_p values consistent with the theoretical prediction within 1σ range. Therefore, we regarded these detections as robust. Velocity deviations in K_p could arise from several physical mechanisms, including 3D

Table 3: Summary of the cross-correlation results.

Species	S/N	K_p (km s^{-1})	Δv (km s^{-1})
<i>Detected signals</i>			
Al I	4.7	$186.0^{+5.7}_{-6.0}$	$4.9^{+2.1}_{-2.3}$
AlH	3.7	185.2 ± 8.3	$-1.0^{+2.7}_{-2.8}$
Ca II	5.0	$189.9^{+8.0}_{-20.0}$	$10.7^{+3.2}_{-7.5}$
Cr I	4.4	$200.7^{+7.5}_{-28.4}$	$6.7^{+2.6}_{-10.7}$
Fe I	9.3	$189.8^{+6.1}_{-6.5}$	$2.6^{+2.1}_{-2.0}$
Fe II	3.8	$178.1^{+16.2}_{-8.6}$	$5.6^{+4.3}_{-4.4}$
Mg I	4.3	$182.3^{+31.2}_{-10.5}$	$5.6^{+6.4}_{-10.4}$
Mn I	5.4	$198.2^{+35.1}_{-17.5}$	$0.4^{+4.3}_{-10.6}$
Ti I	5.3	$198.3^{+9.2}_{-9.5}$	$-1.3^{+3.4}_{-2.7}$
<i>Tentative signals</i>			
C I	3.2	$200.7^{+17.4}_{-8.4}$	$3.0^{+6.4}_{-2.9}$
Ca I	4.3	$186.4^{+4.7}_{-4.1}$	$2.0^{+1.6}_{-1.3}$
Na I	4.6	$196.1^{+10.0}_{-9.4}$	$5.6^{+4.0}_{-3.9}$
NaH	4.1	$187.9^{+45.2}_{-22.3}$	$0.3^{+20.7}_{-8.1}$
Ni I	4.4	$172.5^{+80.9}_{-22.9}$	$-1.5^{+26.5}_{-8.1}$

atmospheric structure, atmospheric dynamics, and planetary rotation (e.g., Wardenier et al. 2025). Similarly, Δv offsets can be induced by uncertainties in v_{sys} and atmospheric dynamics such as day-to-night winds. Nevertheless, given the substantial uncertainties in our detection, the presence of these offsets cannot be definitively confirmed from the current observations.

This work presents the first detection of Al I and AlH in an exoplanet’s atmosphere. Previous searches for aluminum had primarily focused on AlO, a species considered a potential condensate forming clouds or hazes in hot exoplanet atmospheres (e.g., Lodders 2002; Wakeford et al. 2017; Pinhas & Madhusudhan 2017). Gandhi & Madhusudhan (2019) also proposed that the presence of AlO in the planetary atmosphere may enhance visible opacity, leading to the absorption of stellar irradiation and the formation of a temperature inversion layer. For instance, von Essen et al. (2019) reported the first tentative detection (3.3σ) of AlO in the UHJ WASP-33b with low-resolution transmission spectra from OSIRIS at the Gran Telescopio Canarias. Subsequently, Chubb et al. (2020), through a re-analysis of *Hubble* WFC3 transmission spectra combined with *Spitzer* data, confirmed the presence of AlO ($>5\sigma$) in WASP-43b, interpreting it as a potential evidence of the disequilibrium processes, such as vertical or horizontal mixing. Additionally, Saba et al. (2022) also reported a potential existence of AlO in WASP-17b using the *Hubble* STIS and WFC3 transmission spectra. However, at the high temperatures characteristic of UHJs, chemical equilibrium models assuming solar abundances predict that Al I and AlH should be significantly more abundant than AlO (Fig. 5). Therefore, future atmospheric characterization efforts targeting aluminum in UHJs should arguably prioritize searches for Al I and AlH, given their expected prominence in these extreme environments.

Due to the high condensation temperature of aluminum ($T_{\text{cond},50\%} = 1653 \text{ K}$, Lodders 2003) and titanium ($T_{\text{cond},50\%} = 1582 \text{ K}$), species containing these elements are expected to predominantly condense and become cold-trapped in the cooler nightside of hot Jupiters or UHJs. For example, the non-detection of Ti in the atmospheres of WASP-76b and WASP-121b, UHJs with lower equilibrium temperatures

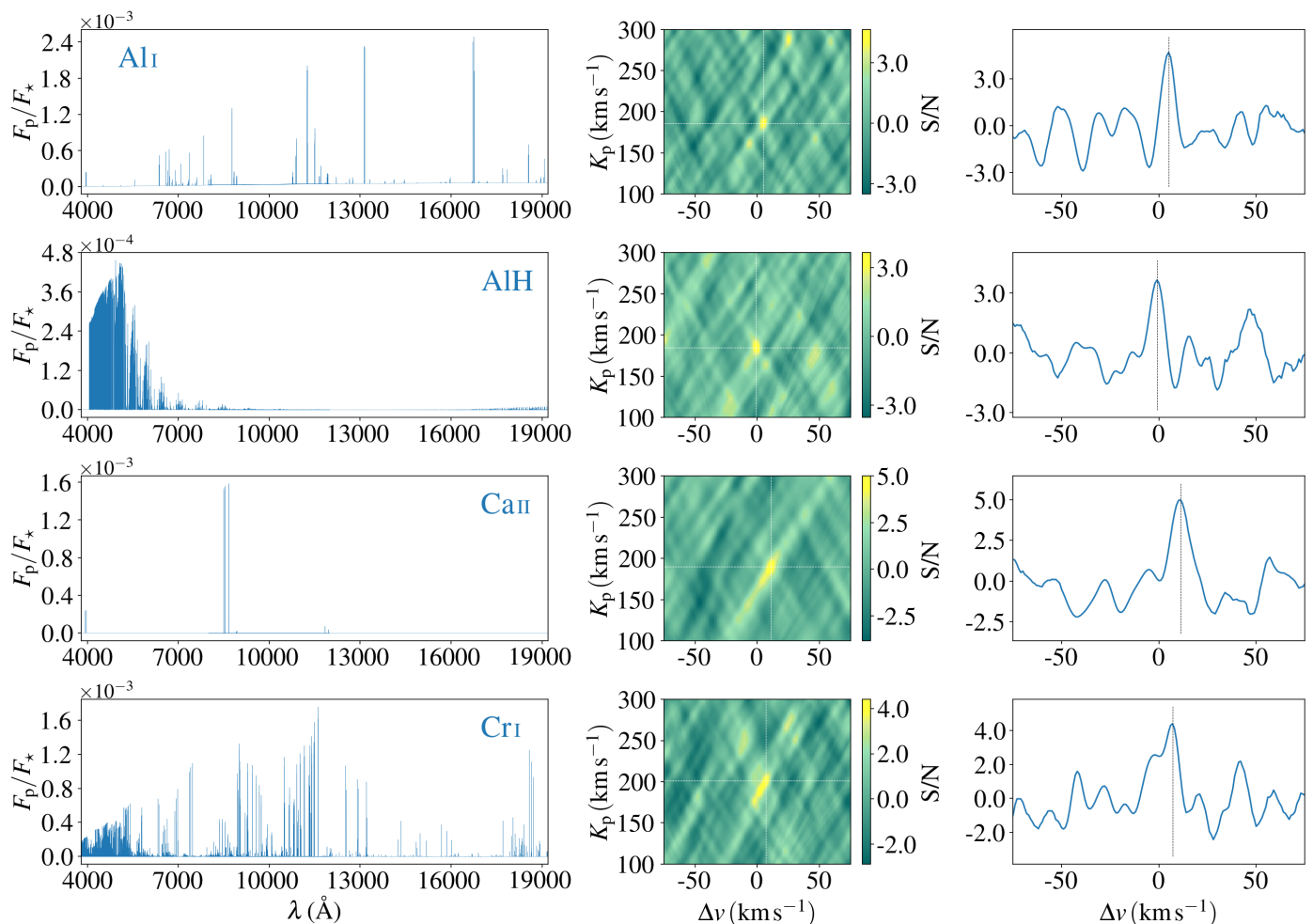


Fig. 2: Model spectra and S/N maps for Al I, Al H, Ca II, and Cr I. *Left panels:* Model spectra for each chemical species. *Middle panels:* Corresponding S/N maps, combining data from both CARMENES and PEPSI instruments. The white dotted lines indicate the position of K_p - $\Delta\nu$ where the S/N reaches its maximum. *Right panels:* CCFs at the K_p values corresponding to the maximum S/N detections.

(WASP-76b: $T_{\text{eq}} = 2231^{+37}_{-36}$ K, Fu et al. 2021; WASP-121b: $T_{\text{eq}} = 2358 \pm 52$ K, Delrez et al. 2016), has been attributed to this type of nightside cold trap. Conversely, several studies have reported detections of Ti I and Ti O in hotter UHJs (Cont et al. 2022; Prinoth et al. 2022; Scandariato et al. 2023; Guo et al. 2024), such as WASP-33b, WASP-189b, and MASCARA-1b (WASP-33b: $T_{\text{eq}} = 2781.7 \pm 41.1$ K, Chakrabarty & Sengupta 2019; WASP-189b: $T_{\text{eq}} = 3353^{+27}_{-34}$ K, Lendl et al. 2020; MASCARA-1b: $T_{\text{eq}} = 2594.3^{+1.6}_{-1.5}$ K, Hooton et al. 2022). In addition, Ishizuka et al. (2021) also successfully detected Ti I in HD 149026b, a hot Saturn with $T_{\text{eq}} = 1626^{+69}_{-37}$ K (Southworth 2010), which was interpreted as resulting from both efficient energy redistribution across the planet and a low Bond albedo ($A \sim 0.1$). Thus, the detection of Al I, Al H, and Ti I in the day-side hemisphere of HAT-P-70b may be attributed to a combination of factors: its high equilibrium temperature and potentially efficient energy and materials transport between the planetary day and night sides hemisphere.

To investigate potential atmospheric heterogeneity on HAT-P-70b, we calculated and compared S/N maps with the observation segments obtained before (night 2) and after (night 1) the secondary eclipse, respectively. We computed model spectra of all detected species and subsequently derived S/N maps

using the methodology detailed in Sect. 3.1. The results are presented in Fig. 6. Prior to secondary eclipse ingress, the peak of the combined signal was located at $K_p = 188.8^{+22.8}_{-24.9}$ km s⁻¹, $\Delta\nu = 2.2^{+7.3}_{-6.4}$ km s⁻¹. After eclipse egress, this peak shifted slightly to $K_p = 186.0^{+45.9}_{-56.2}$ km s⁻¹, $\Delta\nu = 1.3 \pm 19.2$ km s⁻¹. This lack of significant change indicates an absence of large-scale chemical or thermal heterogeneity across the observed dayside hemisphere. This suggests that the atmospheric dynamics of HAT-P-70b are probably not dominated by a strong equatorial super-rotating jet, but rather by day-to-night flow or weak equatorial winds.

We also reported tentative detections of C I, Ca I, Na I, Na H, and Ni I. The presence of C I may result from the thermal dissociation of carbon-bearing molecules such as CO or CH₄ in the high-temperature atmosphere. The C I signal peaks at $K_p = 200.7^{+17.4}_{-8.4}$ km s⁻¹. Although this value is only 13.9 km s⁻¹ redshifted from the theoretical expectation, the 1 σ lower bound is 192.3 km s⁻¹, which excludes the theoretical value from the 1 σ confidence interval. The signals of Ca I and Na I were detected only in the CARMENES data but not in the PEPSI observations with higher S/N values. Similarly, the signals of Na H and Ni I were detected only during the after secondary eclipse phase (night 1), while no significant detection was found during the before secondary eclipse phase (night 2). This discrepancy may be

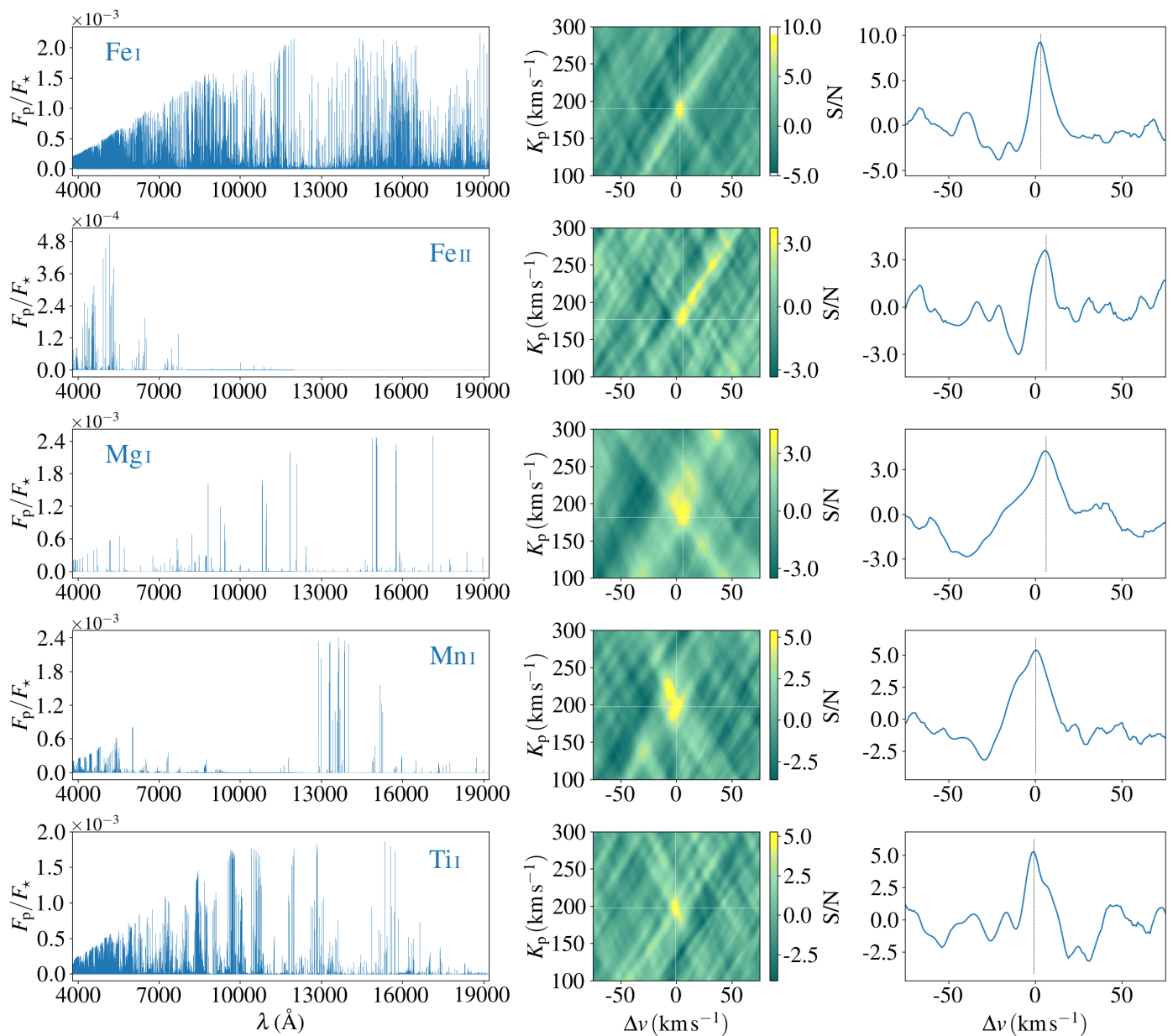


Fig. 3: Same as Fig. 2, but for Fe I, Fe II, Mg I, Mn I, and Ti I.

attributed to the higher S/N of the night 1 data (Table 1). Therefore, we considered these detections to be tentative.

We also applied the same method to search for AlO, Ba I, Ba II, CaH, Co I, Co II, Cr I, Cr II, CrH, FeH, K I, Li I, Mg II, MgH, O I, OH, Sc I, Sc II, Si I, Ti II, TiO, V I, V II, VO, and Y I. However, no significant signals of these species were detected. Several factors may account for these non-detections. First, some species lack dense or strong spectral lines within the observed wavelength range. For instance, certain metal ions (e.g., Co II, Cr II, and V II) exhibit strong spectral lines just in the ultraviolet band. Second, inaccuracies in the opacity database for some species could hinder effective detection. Third, the S/N of the observational data may be insufficient to reveal weak spectral features. Finally, low atmospheric abundance could also explain the absence of detectable signals. For instance, certain species may undergo thermal dissociation in the hot inversion layer, while others may condense in cooler regions or on the nightside, resulting in their depletion from the observable atmosphere.

4. Atmospheric retrieval

4.1. Retrieval methods

Based on the detection results with CCF, we performed atmospheric retrievals to constrain the atmospheric properties with the observed thermal emission spectra. We employed the latest retrieval techniques for high-resolution spectroscopy, as described in Yan et al. (2023).

The forward models were computed using `petitRADTRANS`, adopting a free T - P profile to describe the atmospheric structure. The T - P profile was parameterized by nine free temperature points (T_8 - T_0) uniformly distributed in log-pressure coordinates between 10^{-8} bar (uppermost altitude point, T_8) and 10^0 bar (lowermost altitude point, T_0), with each point set as a free parameter ranging from 100 K to 6000 K. Following the methodology of Pelletier et al. (2021), we imposed a Gaussian prior with a smoothing strength of $\sigma_s = 150 \text{ K dex}^{-2}$ to prevent nonphysical zig-zaggy temperature oscillations across pressure

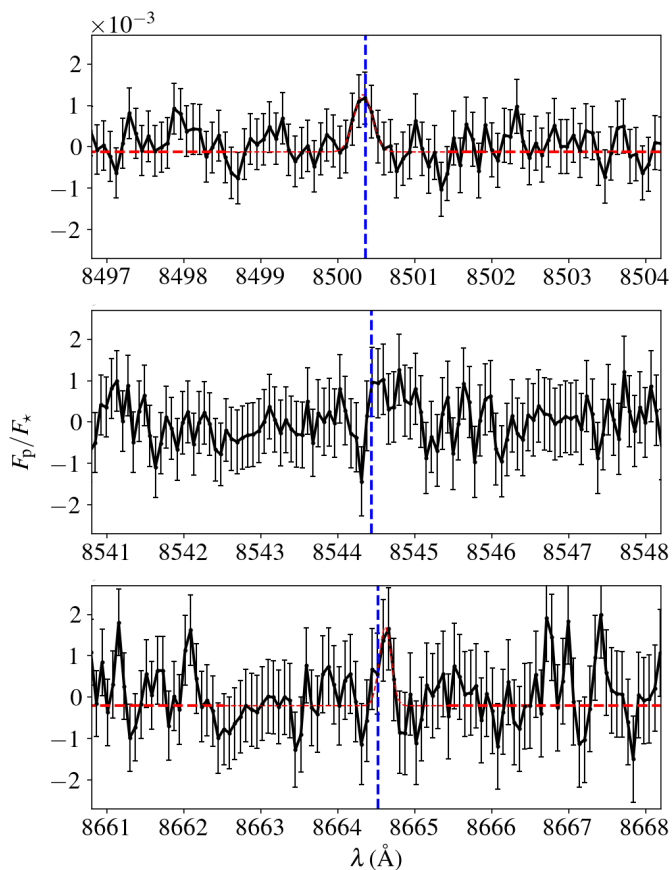


Fig. 4: Ca II triplet emission lines observed with PEPSI. They were combined over two nights and shifted to the planetary rest frame using the best-fit velocity from the Ca II CCF signal. The dashed blue lines indicate the expected positions of the Ca II triplet lines. Among them, only the lines near 8500.36 Å and 8664.52 Å (vacuum wavelengths) were detected, with their Gaussian fits in red.

scales. The atmospheric structure in `petitRADTRANS` was divided into 51 discrete layers, uniformly sampled in log-pressure space from the upper boundary at 10^{-8} bar to the lower boundary at 10^0 bar. The normalization of models was consistent with the description in Sect. 3.1.

For the volume mixing ratio (VMR) of the chemical species, we employed two different methods. The first method, chemical free retrieval (FR), assumed that the VMR of each chemical species remained constant across all atmospheric layers. In this case, the logarithm of the VMR for each species, such as $\log(\text{Al I})$ and $\log(\text{Fe I})$, was treated as a free parameter. The second method, chemical equilibrium retrieval (ER), set the relative abundance of each element (e.g., $[\text{Al}/\text{H}]$, $[\text{Fe}/\text{H}]$) as a free parameter, defined by

$$[\text{X}/\text{H}] = \log(X_p) - \log(X_\odot) = \log\left(\frac{X_p}{X_\odot}\right), \quad (4)$$

where X represents a given element (e.g., Al, Fe), and $\log(X_p)$ and $\log(X_\odot)$ denote the logarithmic VMRs of the element in the planetary and solar compositions, respectively. For the ER method, we utilized the open-source chemical equilibrium code `pyFastChem` (Stock et al. 2022) to calculate the VMRs of all species and the mean molecular weight in each atmosphere layer,

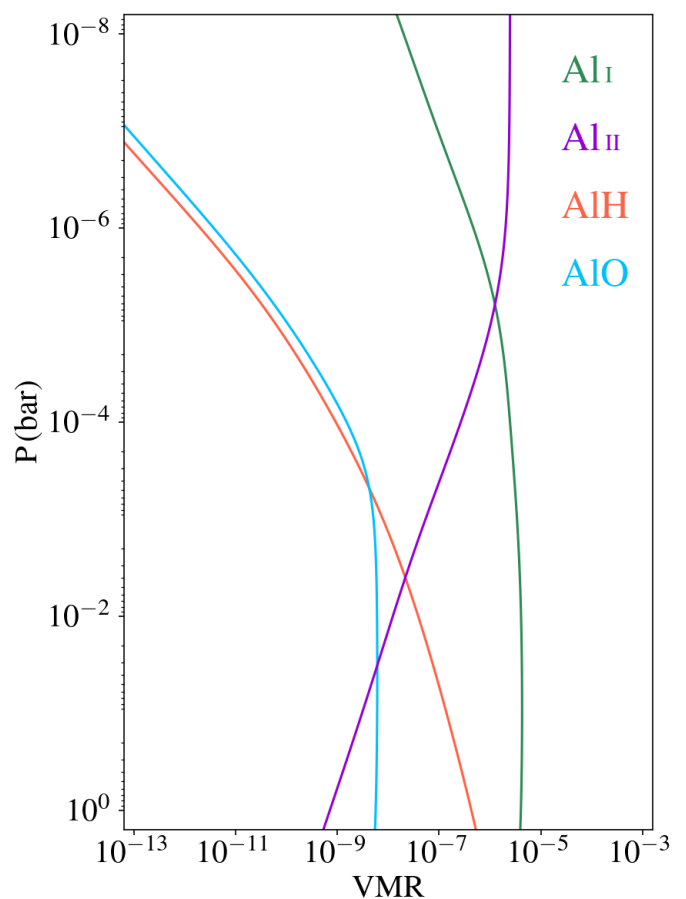


Fig. 5: Volume mixing ratios of Al I, Al II, AlO, and AlH as a function of pressure, calculated under the assumption of chemical equilibrium. An isothermal temperature profile of 2500 K was adopted.

based on retrieval parameters such as temperature profile and elemental abundance. During chemical equilibrium calculations, we considered 29 elements and the free electrons. The abundances of Al, C, Ca, Cr, Fe, Mg, Mn, Na, Ni, Ti, and V were treated as free parameters, while the abundances of all other elements not targeted in the retrieval were fixed to their solar values. These calculations included 531 chemical species, comprising 501 molecular and ionic species such as CO, FeH, Ti II, and V II. Condensation processes at low temperatures were excluded from the modelling framework, as they are negligible in the extreme temperature of UHJs while also simultaneously reducing computational cost.

Accurate modelling of spectral line broadening is critical for atmospheric retrieval. The pressure and thermal broadening were already included in the calculation of the opacity linelist. Additionally, we convolved the model spectra with a Gaussian profile corresponding to the resolution of the spectrograph. To account for planetary rotation, we further incorporated rotational broadening using the profile described by Díaz et al. (2011) and convolved it to the model spectra,

$$G(x) = \frac{2(1-\varepsilon)(1-x^2)^{\frac{1}{2}} + \frac{\pi\varepsilon}{2}(1-x^2)}{\pi(1-\frac{\varepsilon}{3})}, \quad (5)$$

$$x = \ln\left(\frac{\lambda}{\lambda_0}\right) \cdot \frac{c}{v_{\text{eq}} \sin i_p},$$

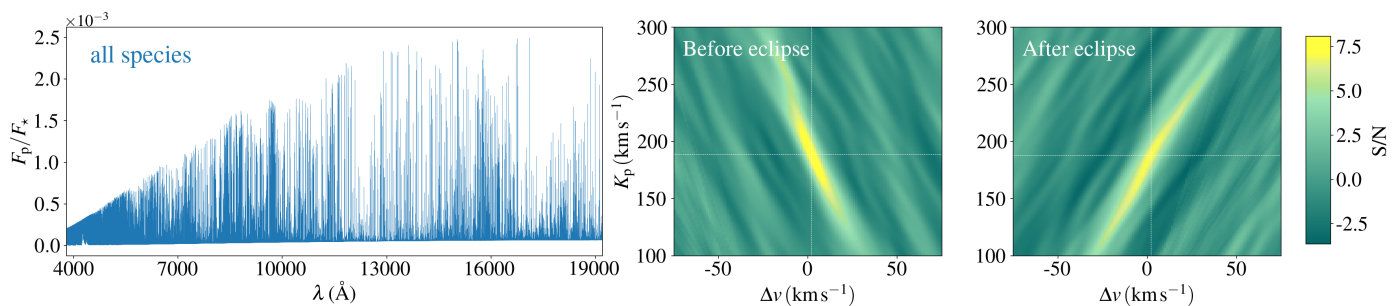


Fig. 6: *Left panel*: Model spectra obtained by combining all detected species (i.e., Al I, Al H, Ca II, Cr I, Fe I, Fe II, Mg I, Mn I, Ti I). *Middle and right panels*: S/N maps corresponding to the orbital phase before (night 2) and after (night 1) eclipse, respectively. Dashed white lines mark the locations of the best-fit K_p and Δv values.

where λ_0 is the central wavelength of the spectral line, ε is the limb darkening coefficient, and v_{eq} is the equatorial rotation velocity. We adopted a linear limb darkening model and set the ε to 1, completely neglecting contributions from the planetary limb to the total radiation flux. Assuming tidal locking for HAT-P-70b, we fixed v_{eq} at 3.46 km s^{-1} , consistent with synchronous rotation at the system's orbital period. To mitigate the smearing effect caused by the planetary orbital motion during the exposure time, the model spectra were further convolved with a box function in velocity space (i.e., $\ln \lambda$), with the width of the box corresponding to the planetary RV change of approximately 1.5 km s^{-1} over the course of the ~ 5 -min exposure. Furthermore, we applied the fast SYSREM filtering algorithm to the model spectra to obtain the final model spectral matrix, following the methodology outlined in Sect. 3.1.2, with K_p and Δv treated as free parameters. Finally, a Gaussian high-pass filter with a Gaussian σ of 31 points was applied to both the final residual and model spectral matrices to remove any remaining broadband features.

We performed atmospheric retrieval by sampling the posterior distribution using the Markov chain Monte Carlo (MCMC) ensemble sampler emcee (Foreman-Mackey et al. 2013). The logarithm likelihood function was defined as

$$\ln \mathcal{L} = - \sum_{ij} \left[\frac{(R_{ij} - M_{ij})^2}{(\beta \sigma_{ij})^2} + \ln(2\pi(\beta \sigma_{ij})^2) \right], \quad (6)$$

where R_{ij} and M_{ij} denote the residual and model spectral matrices respectively, σ_{ij} represents the residual noise matrix, and β are scaling factors accounting for the noise. We ran the MCMC simulation with 20 000 steps and 200 walkers for each parameter. In the MCMC sampling procedure, the initial 10 000 steps were discarded as burn-in to ensure adequate convergence of the Markov chains.

4.2. Retrieval results

4.2.1. Basic retrieved parameters

Our retrievals were performed independently for the FR and ER. The posterior distribution corner maps are presented in Figs. A.2 and A.3.

The retrieved T - P profiles are shown in Fig. 8. The ER results indicate the presence of a temperature inversion layer between 10^{-1} and 10^{-5} bar, with a temperature difference of approximately 1700 K. In contrast, the FR results suggest a more complex, double-inversion structure. The lower inversion layer (10^{-1} to 10^{-3} bar) is likely retrieved from the neutral metal lines

such as Fe I, while the higher inversion layer (10^{-5} to 10^{-7} bar) is plausibly retrieved from ionized metal lines (e.g., Fe II and Ca II). Additionally, we employed a modified version of the HELIOS code (Malik et al. 2017) to compute a self-consistent atmospheric model. A detailed description of the HELIOS model calculation can be found in Yan et al. (2022b). Due to the relatively large uncertainties in the retrieved profile, the HELIOS model shows agreement with the retrieval results, except in the uppermost atmosphere (10^{-7} to 10^{-8} bar), where discrepancies are more pronounced.

Both K_p and Δv were included as free parameters in all retrievals. The FR yields a K_p value of $187.9_{-1.1}^{+1.2} \text{ km s}^{-1}$, while the ER result is $187.7_{-1.1}^{+1.2} \text{ km s}^{-1}$, both consistent with the values obtained from CCF. Although the best-fit values show a slight deviation of $\sim 1.0 \text{ km s}^{-1}$ relative to the theoretical expectation, these offsets lie within the 1σ uncertainty range. The retrieved Δv is $2.19_{-0.40}^{+0.37} \text{ km s}^{-1}$ for FR and $2.15_{-0.36}^{+0.37} \text{ km s}^{-1}$ for ER, both indicating a redshift of approximately 2.0 km s^{-1} . This redshift may be attributed to day-to-night atmospheric winds on the planet, although uncertainties of v_{sys} and transit ephemeris can also contribute to the Δv shift (Meziani et al. 2025).

For the metal abundance, the FR yielded a Fe I VMR of $\log(\text{Fe I}) = -4.16_{-1.11}^{+0.74}$, corresponding to a metallicity of $[\text{Fe}/\text{H}] = 0.38_{-1.11}^{+0.74}$. In contrast, the ER gave a metallicity of $[\text{Fe}/\text{H}] = 0.23_{-0.98}^{+1.08}$. Both retrieved metallicity values are consistent with the solar value within the 1σ range.

4.2.2. Elemental abundance pattern

From the MCMC posterior samples, we derived the solar-relative abundance for each element ($[X/\text{H}]$) and subsequently converted them into iron-relative abundances ($[X/\text{Fe}]$):

$$[X/\text{Fe}] = \log\left(\frac{X_p}{X_\odot}\right) - \log\left(\frac{\text{Fe}_p}{\text{Fe}_\odot}\right) = [X/\text{H}] - [\text{Fe}/\text{H}]. \quad (7)$$

These results are presented in Fig. 9 for FR and Fig. 10 for ER, with the specific values summarized in Table A.2. In the FR results, the abundance of Al was determined by both Al I and Al H, whereas the abundances of all other elements were inferred solely from their atomic species, implying an underlying assumption that these elements are predominantly in atomic form.

The retrieved abundance of Na appears slightly subsolar, likely due to thermal dissociation and ionization at high temperatures. This element are highly prone to ionization and their ionic forms may dominate in the atmosphere, causing the atomic-based retrievals to significantly underestimate their true abun-

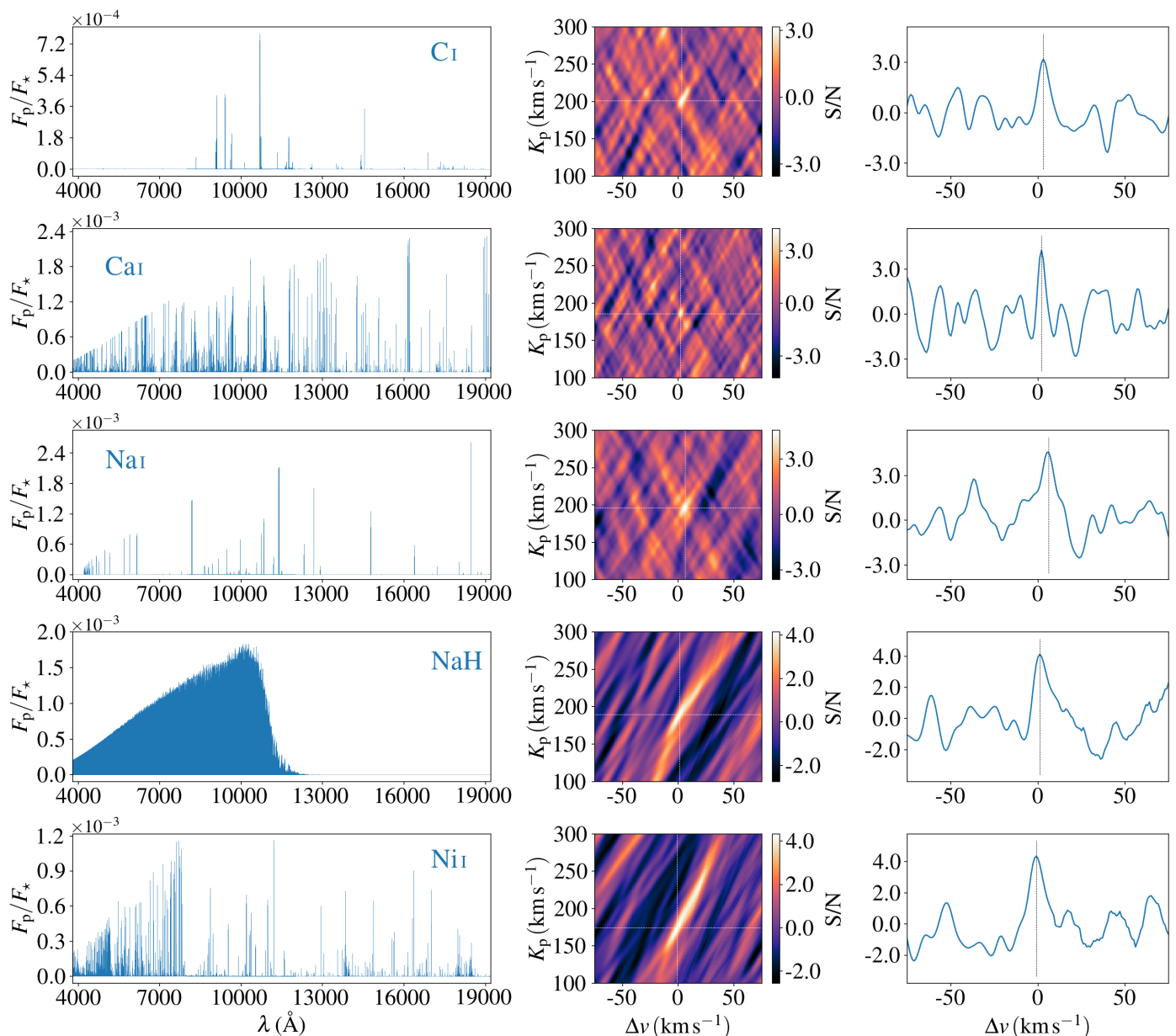


Fig. 7: Same as Fig. 2 but showing tentative detections. The S/N maps for Ca I and Na I are derived exclusively from CARMENES spectra, whereas those for Na H and Ni I only use the first night data.

dances. V was not detected, with the retrieval providing only a 1σ upper limit of $\log(V) < -9.69$, which is substantially below the solar value ($\log(V)_{\odot} = -8.04$). For Ti, its high condensation temperature suggests potential condensation on the planet’s cooler nightside. However, efficient atmospheric circulation likely transports Ti-bearing species to the dayside hemisphere of HAT-P-70b, resulting in only a mild depletion with a Ti abundance slightly below solar. The abundances of all other elements are consistent with solar values within the 1σ range.

Based on the high-resolution transmission spectra observed by HARPS-N, Gandhi et al. (2023) also retrieved the abundances of various metal species in the atmosphere of HAT-P-70b using the FR method. Most of the retrieved abundances show a good agreement within 1σ between the two works. Only the abundance of Cr shows notable difference, but the values are still within the 2σ uncertainty range.

Our ER analysis, which accounts for thermal ionization, yields a Na abundance consistent with the solar value. Similarly, the abundances of Mn, Cr, and Mg also align with solar abundances, corroborating the findings from our FR results. Among all retrieved elements, Ni is the only one showing a significantly super-solar abundance, with $[\text{Ni}/\text{Fe}] = 1.01^{+0.50}_{-0.60}$. This Ni enrichment, also observed on another UHJ, namely WASP-76b (Pelletier et al. 2023), may be attributed to the accretion of Ni-rich planetesimals during the planet’s formation. For refractory elements with high condensation temperatures ($T_{\text{cond},50\%} > 1400$ K), such as V, Ca, and Ti, the inferred abundances are modestly depleted, consistent with the FR findings. In the case of Al, which has the highest condensation temperature among the retrieved elements, no significant depletion is observed. This may be due to disequilibrium processes, with a substantial fraction of Al stored in molecular form (e.g., AlH). Alternatively, the planet may have formed with an inherent en-

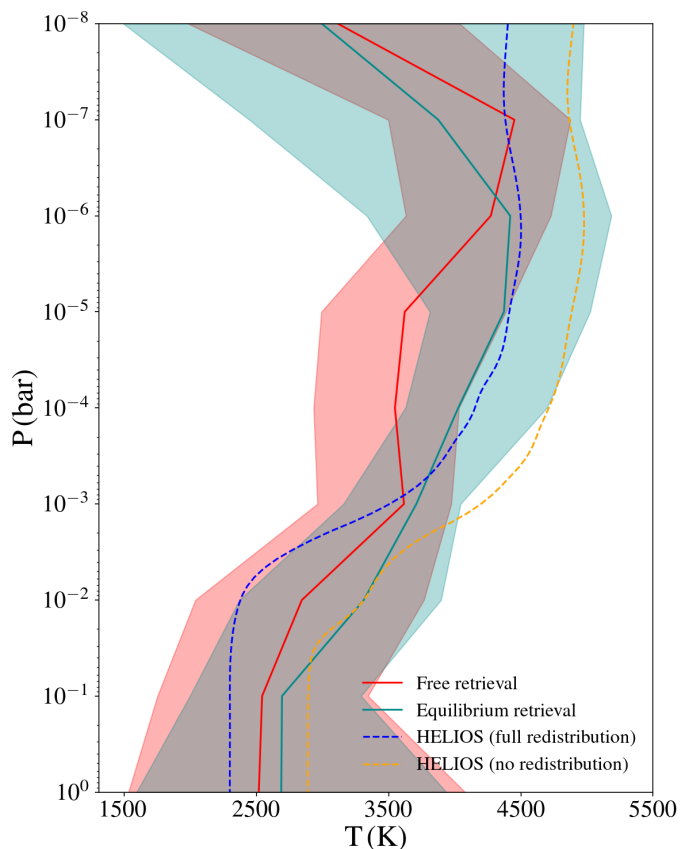


Fig. 8: Retrieved T - P profile (solid line) compared with predictions from the self-consistent HELIOS model (dashed line). The HELIOS model assumes solar elemental abundances and considers two scenarios: no heat redistribution (dayside only) and full heat redistribution between the dayside and nightside. The shaded regions indicate the 1σ confidence interval of the retrieved profile.

richment of Al (similarly to Ni) and despite being potentially depleted due to cold-trapping, the dayside hemispheric Al abundance could still appear consistent with the solar value as a result.

Compared to the FR results, the uncertainties on the abundances derived from the ER are smaller, suggesting that the chemical equilibrium assumption more accurately represents the atmospheric condition of HAT-P-70b. Furthermore, the ER consistently yields higher abundances for most elements compared to the FR (Table A.2), which is a natural result of metal ionization. As shown in Fig. 11, the VMRs of most metals significantly drop towards lower pressures due to strong ionization in the upper planetary atmosphere. Therefore, the free retrieval, which only accounts for atomic species, tends to underestimate the abundances. The only exception is Mg, which has similar retrieved abundances between ER and FR. This is not surprising because Mg and Fe are known to be less prone to ionization, as suggested by chemical equilibrium calculations (Fig. 11).

We also attempted to constrain the abundance of C using the tentative detection of C I. The FR results suggested an upper limit of $\log(C I) < -3.09$ (corresponding to $[C/H] < 0.56$). The ER yielded a tighter constraint of $[C/H] < 0.74$. Since the retrieval cannot constrain well the abundance and only an upper limit is yielded, we considered the tentative C I signal as a possible false positive.

It is also important to note that the detection of a species in the planetary atmosphere does not necessarily imply that the corresponding element is not depleted. For example, although we detected a $S/N \sim 5.3$ emission signal for Ti I with CCF, the retrievals still yielded a subsolar Ti abundance (FR: $[Ti/Fe] = -1.51^{+0.56}_{-0.74}$, ER: $[Ti/Fe] = -0.85^{+0.55}_{-0.63}$). This highlights that a definitive assessment of elemental depletion should rely on quantitative abundance retrieval rather than detection significance alone.

4.2.3. Evidence of disequilibrium processes

Our FR independently constrained the abundances of each species, revealing some results inconsistent with chemical equilibrium models. Notably, the retrieved VMRs for ionized species were unexpectedly high: $\log(Ca II) = -1.75^{+0.95}_{-2.07}$ and $\log(Fe II) = -2.50^{+1.12}_{-1.23}$. The relative abundances between atomic and ionic species were also calculated. The results showed that the VMR of Ca I exceeds that of Ca II by approximately seven orders of magnitude ($\log(Ca II/Ca I) = 7.24^{+3.91}_{-2.16}$), while the VMR of Fe II is about two orders of magnitude greater than that of Fe I ($\log(Fe II/Fe I) = 1.80^{+0.64}_{-0.69}$). The posterior distributions for these species are shown in Fig. 12.

These discrepancies may arise from some disequilibrium processes, predominately the hydrodynamic expanding effect. In the above retrievals, we assumed the atmosphere to be hydrostatic. However, UHJs could have strong atmospheric escape with outward-expanding flow (Yan et al. 2019; Sing et al. 2019). This type of hydrodynamic process significantly enhances the atmospheric density at high altitudes. Since the detected lines of the ionized species are likely formed at high altitudes, this hydrodynamic effect is more prominent for ionic lines compared to the atomic lines. Thereby, our retrieval under hydrostatic assumption tends to compensate this effect by enhancing the VMRs of Ca II and Fe II to extremely exaggerated values. Further atmosphere modeling work that would include hydrodynamic escape could help resolve the discrepancies and provide a credible mass loss rate (Huang et al. 2023).

Furthermore, our analysis relies on forward models calculated under the assumption of local thermodynamic equilibrium (LTE), which neglects potential non-LTE (NLTE) effects. As demonstrated by Fossati et al. (2021), NLTE effects can alter the population distribution of atomic energy levels for metals (e.g., Fe and Mg) in the atmospheres of UHJs, thereby impacting both the atmospheric thermal structure and the strength of spectral lines. For example, NLTE effects may enhance certain spectral features, such as Fe II lines, beyond the predictions of an LTE model. Consequently, an atmospheric retrieval framework built upon LTE assumptions may erroneously compensate for these stronger-than-expected lines by overestimating the VMRs of metal species to fit the observed spectra.

5. Conclusions

We observed the dayside thermal emission spectra of the UHJ HAT-P-70b with the high-resolution spectrographs CARMENES and PEPSI, both covering orbital phases before and after the secondary eclipse. Atmospheric features were identified using the CCF method, followed by atmospheric retrievals to constrain the elemental abundances and the dayside T - P profile. Our main conclusions are summarized below:

- We detected the emission signals of Al I, Al II, Ca II, Cr I, Fe I, Fe II, Mg I, Mn I, and Ti I. This marks the first detection of Al I

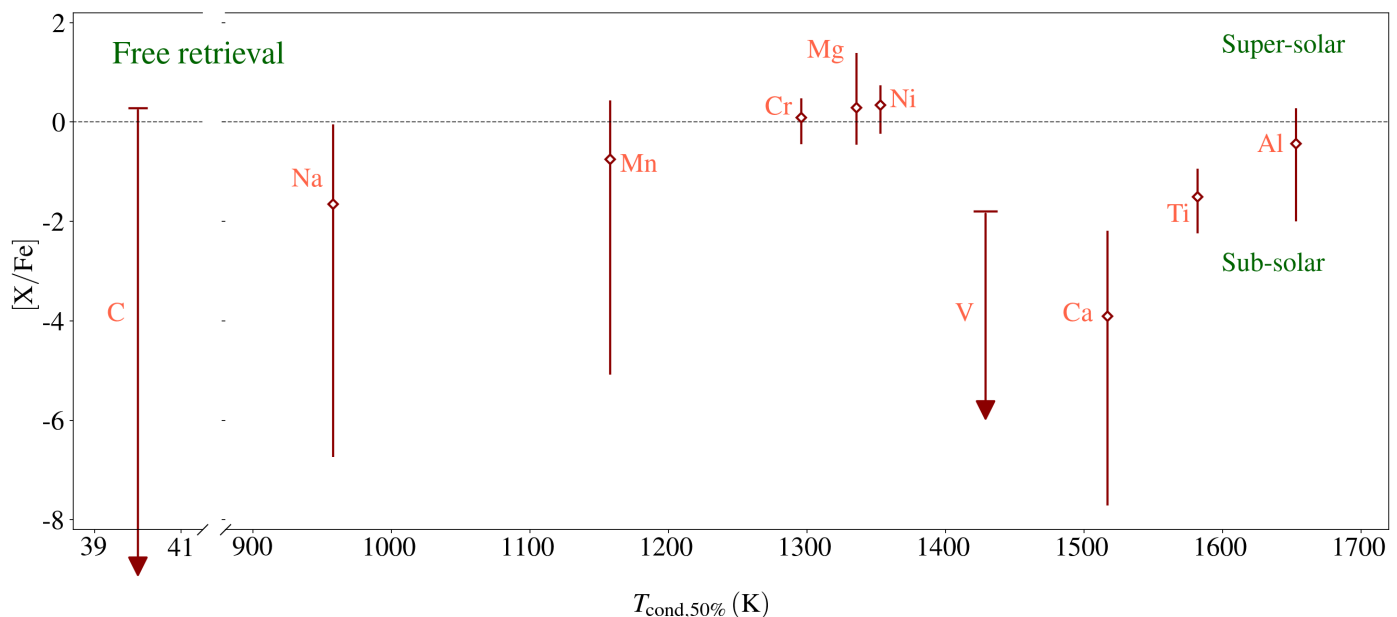


Fig. 9: Elemental abundances in the atmosphere of HAT-P-70b relative to iron, derived from chemical free retrieval, as a function of condensation temperature. The dashed black line represents consistency with solar abundance. All error bars indicate 1σ uncertainties, while the abundances of C and V are reported as upper limits.

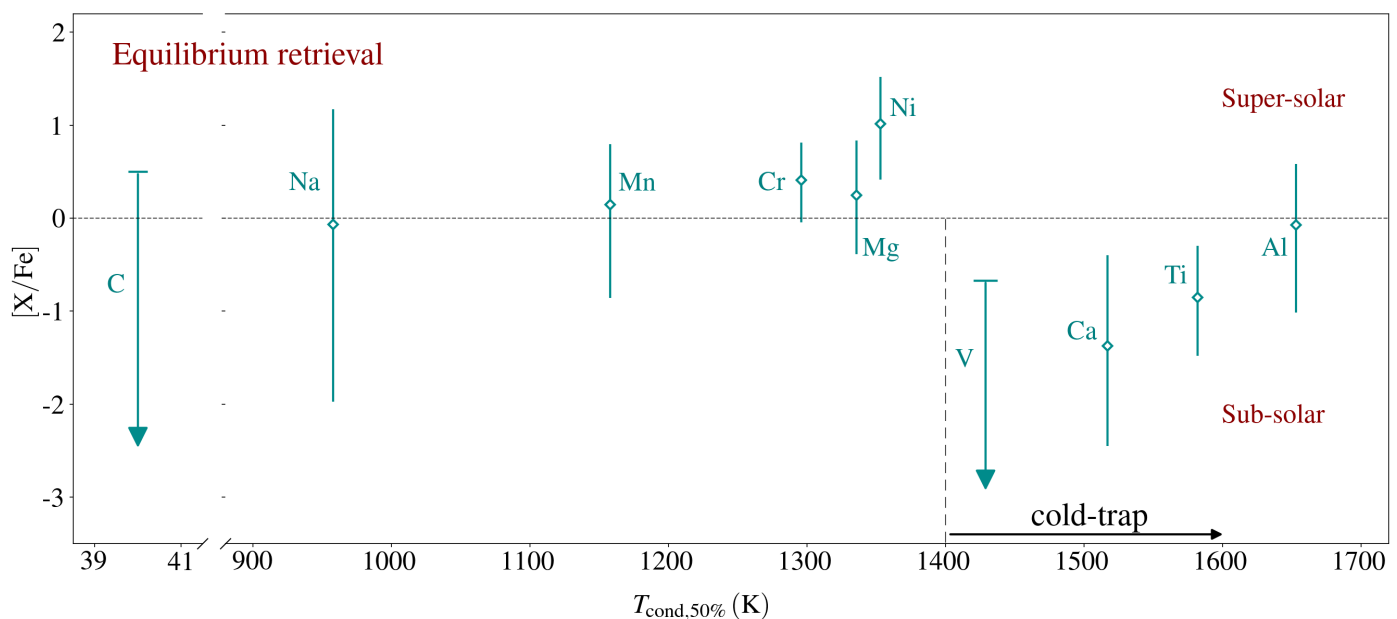


Fig. 10: Same as Fig. 9 but for chemical equilibrium retrieval results.

and AlH in an exoplanet's atmosphere. We also presented tentative detections of C I, Ca I, Na I, NaH, and Ni I.

- Given the high condensation temperature of aluminum and titanium, the detections of Al I, AlH, and Ti I imply efficient energy and materials transport between the day and night side hemispheres of HAT-P-70b. Furthermore, our findings suggest that AlH is a more prominent aluminum reservoir than AlO in UHJ atmospheres, highlighting its importance for future atmospheric characterization efforts.
- A combined CCF analysis incorporating all detected species revealed no significant velocity offset between before and after the secondary eclipse observations, suggesting no strong longitudinal heterogeneity. This suggests that the atmo-

spheric dynamics of HAT-P-70b are likely not dominated by a strong equatorial super-rotating jet.

- We independently performed FR and ER to constrain the planet's atmospheric properties. Both retrieval frameworks consistently identified a strong thermal inversion in the dayside hemisphere, with a temperature increase of ~ 1500 – 2000 K between the lower and the upper planetary atmosphere.
- The retrieved metallicity $[Fe/H]$ is $0.38^{+0.74}_{-1.11}$ from FR and $0.23^{+1.08}_{-0.98}$ from ER. The abundances of Na, Mn, Cr, and Mg are consistent with solar values, whereas those of V, Ca, and Ti appear moderately depleted, likely as a consequence of cold-trapping on the planet's cooler nightside, owing to their

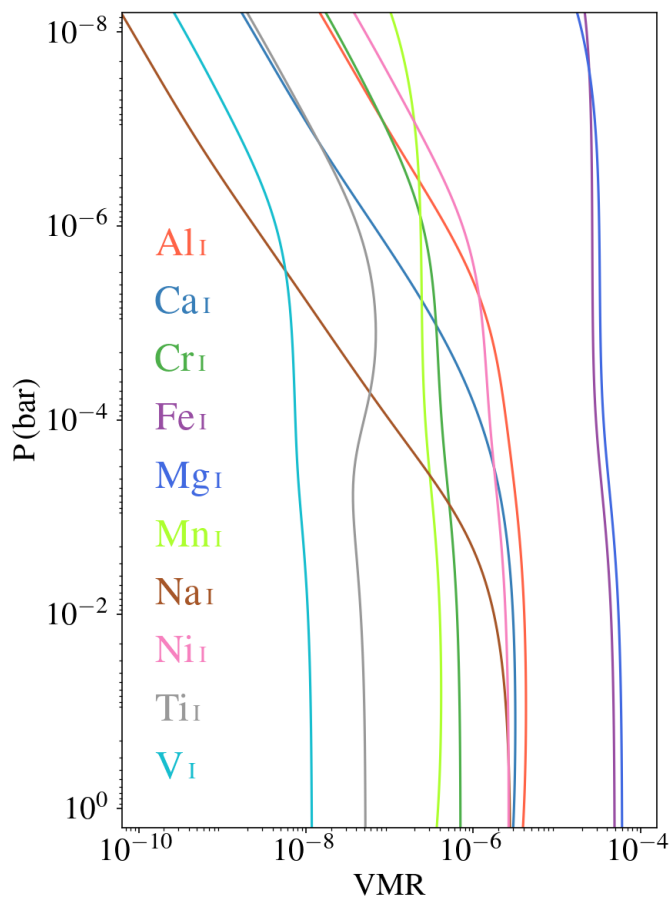


Fig. 11: Volume mixing ratios of all targeted metal atoms as a function of pressure at a fixed isothermal temperature of 2500 K under the assumption of chemical equilibrium. All elemental abundances are assumed to be solar. The results are illustrative calculations intended to demonstrate metal ionization, rather than retrieval results.

high condensation temperatures ($T_{\text{cond},50\%} > 1400$ K). Notably, Ni shows a tentatively mild enrichment, which may be attributed to the accretion of Ni-rich planetesimals during the planet’s formation and evolution. In particular, Al, despite having the highest condensation temperature, exhibits an abundance consistent with the solar value, which could be due to its initial enrichment during formation.

- The FR analysis, which independently constrained the VMRs of atoms and ions, revealed significantly high abundances of ionized species such as Fe II and Ca II. These results strongly deviate from chemical equilibrium predictions under hydrostatic assumption, indicating the high altitude atmosphere is likely undergoing significant hydrodynamic escaping.

In this work, we present the first dayside observation of HAT-P-70b, with the discovery of a rich array of spectral features characterizing refractory species. The elemental abundance pattern of these detected species offers important insight into the planet’s formation and evolutionary history. However, our observations were primarily conducted in the visible band and lack a high-quality IR data to detect volatile species such as CO. As a result, the C/O ratio remains poorly constrained. Future observations using ground-based high-resolution IR spectrographs (e.g., CRIRES+, IGRINS, IGRINS-2) or space-based facilities such

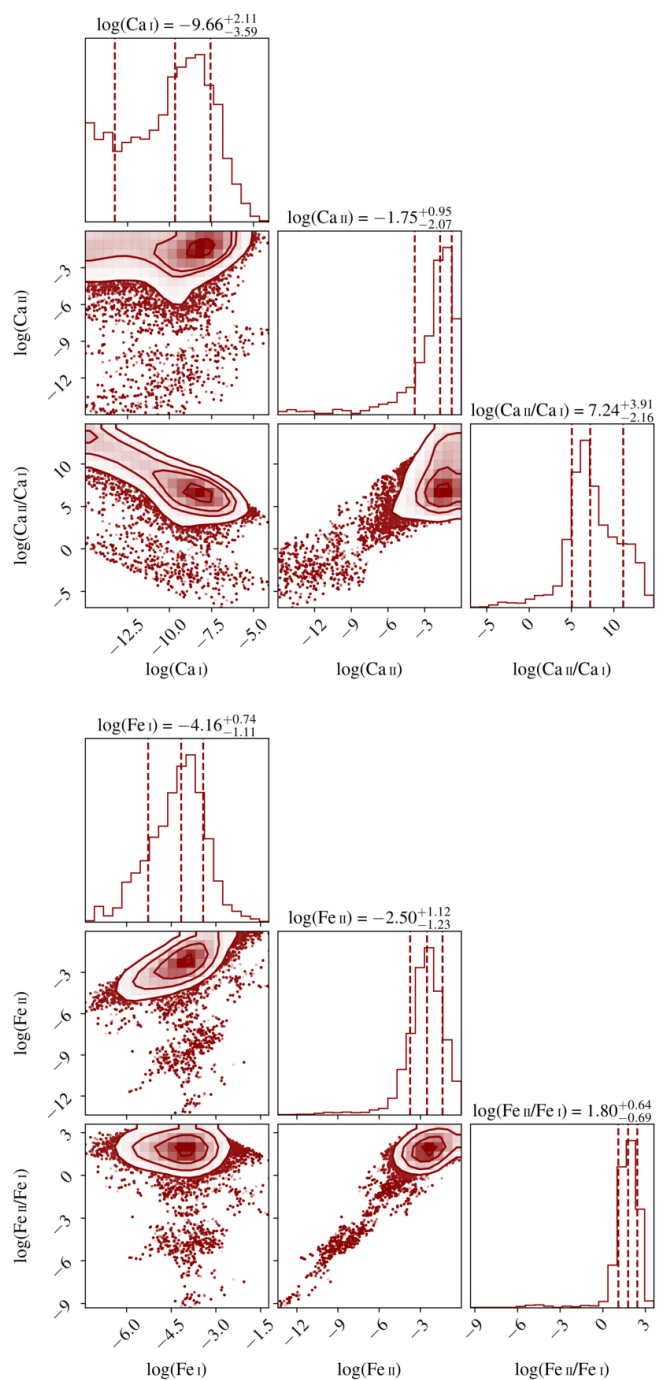


Fig. 12: Posterior distribution corner plots for the VMRs of Ca I and Ca II (top), and Fe I and Fe II (bottom), obtained from the chemical free retrieval results. The relative abundances between these species are also calculated.

as JWST could provide a more comprehensive characterization of the planet’s elemental abundance pattern.

Acknowledgements. We acknowledge the support by the National Natural Science Foundation of China (grant no. 42375118). This publication was based on observations collected under the CARMENES Legacy+ project. CARMENES is an instrument at the Centro Astronómico Hispano en Andalucía (CAHA) at Calar Alto (Almería, Spain), operated jointly by the Junta de Andalucía and the Instituto de Astrofísica de Andalucía (CSIC). Funding for CARMENES has been provided by the Max-Planck-Institut für Astronomie (MPIA), Consejo Superior de Investigaciones Científicas (CSIC), European Regional De-

velopment Fund (ERDF), Ministerio de Ciencia, Innovación y Universidades (MICIU), Deutsche Forschungsgemeinschaft (DFG) and the members of the CARMENES Consortium (<https://carmenes.caha.es>). The LBT is an international collaboration among institutions in the United States, Italy and Germany. LBT Corporation partners are: The University of Arizona on behalf of the Arizona Board of Regents; Istituto Nazionale di Astrofisica, Italy; LBT Beteiligungsgesellschaft, Germany, representing the Max-Planck Society, The Leibniz Institute for Astrophysics Potsdam, and Heidelberg University; The Ohio State University, representing OSU, University of Notre Dame, University of Minnesota and University of Virginia. We thank the German Federal Ministry (BMBF) for the year-long support for the construction of PEPSI through their Verbundforschung grants 05AL2BA1/3 and 05A08BAC as well as the State of Brandenburg for the continuing support of PEPSI for the LBT (<https://pepsi.aip.de/>). We acknowledge financial support from the Agencia Estatal de Investigación (AEI/10.13039/501100011033) of the MICIU and the ERDF “A way of making Europe” through projects PID2022-137241NB-C4[1:4], PID2021-125627OB-C3[1:2], PID2021-126365NB-C21, and the Centre of Excellence “Severo Ochoa” and “María de Maeztu” awards to the Instituto de Astrofísica de Andalucía (CEX2021-001131-S) and Institut de Ciències de l’Espai (CEX2020-001058-M). D.C. is supported by the LMU-Munich Fraunhofer-Schwarzschild Fellowship and by the Deutsche Forschungsgemeinschaft (DFG, German Research Foundation) under Germany’s Excellence Strategy – EXC 2094 – 390783311. This work was co-funded by the European Union (ERC-CoG, EVAPORATOR, Grant agreement No. 101170037). Views and opinions expressed are however those of the author(s) only and do not necessarily reflect those of the European Union or the European Research Council. Neither the European Union nor the granting authority can be held responsible for them.

References

- Bello-Arufe, A., Cabot, S. H. C., Mendonça, J. M., Buchhave, L. A., & Rathcke, A. D. 2022, *AJ*, 163, 96
- Bernath, P. F. 2020, *Journal of Quantitative Spectroscopy and Radiative Transfer*, 240, 106687
- Brooke, J. S., Bernath, P. F., Western, C. M., et al. 2016, *Journal of Quantitative Spectroscopy and Radiative Transfer*, 168, 142
- Burrows, A., Ram, R. S., Bernath, P., Sharp, C. M., & Milsom, J. A. 2002, *ApJ*, 577, 986
- Caballero, J. A., Guàrdia, J., López del Fresno, M., et al. 2016, in *Society of Photo-Optical Instrumentation Engineers (SPIE) Conference Series*, Vol. 9910, *Observatory Operations: Strategies, Processes, and Systems VI*, ed. A. B. Peck, R. L. Seaman, & C. R. Benn, 99100E
- Chachan, Y., Knutson, H. A., Lothringer, J., & Blake, G. A. 2023, *ApJ*, 943, 112
- Chakrabarty, A. & Sengupta, S. 2019, *AJ*, 158, 39
- Choi, Y.-H., Jeong, U., Lee, J.-J., et al. 2025, *AJ*, 170, 238
- Chubb, K. L., Min, M., Kawashima, Y., Helling, C., & Waldmann, I. 2020, *A&A*, 639, A3
- Cont, D., Nortmann, L., Lesjak, F., et al. 2025, *A&A*, 698, A31
- Cont, D., Nortmann, L., Yan, F., et al. 2024, *A&A*, 688, A206
- Cont, D., Yan, F., Reiners, A., et al. 2021, *A&A*, 651, A33
- Cont, D., Yan, F., Reiners, A., et al. 2022, *A&A*, 668, A53
- Cridland, A. J., van Dishoeck, E. F., Alessi, M., & Pudritz, R. E. 2019, *A&A*, 632, A63
- Cridland, A. J., van Dishoeck, E. F., Alessi, M., & Pudritz, R. E. 2020, *A&A*, 642, A229
- Czesla, S., Lampón, M., Cont, D., et al. 2024, *A&A*, 683, A67
- Czesla, S., Schröter, S., Schneider, C. P., et al. 2019, *PyA: Python astronomy-related packages*, *Astrophysics Source Code Library*, record ascl:1906.010
- Delrez, L., Santerne, A., Almenara, J. M., et al. 2016, *MNRAS*, 458, 4025
- Díaz, C. G., González, J. F., Levato, H., & Grosso, M. 2011, *A&A*, 531, A143
- Evans-Soma, T. M., Sing, D. K., Barstow, J. K., et al. 2025, *Nature Astronomy*, 9, 845
- Finnerty, L., Xin, Y., Xuan, J. W., et al. 2025, *AJ*, 169, 333
- Foreman-Mackey, D., Hogg, D. W., Lang, D., & Goodman, J. 2013, *PASP*, 125, 306
- Fortney, J. J., Lodders, K., Marley, M. S., & Freedman, R. S. 2008, *ApJ*, 678, 1419
- Fossati, L., Young, M. E., Shulyak, D., et al. 2021, *A&A*, 653, A52
- Fu, G., Deming, D., Lothringer, J., et al. 2021, *AJ*, 162, 108
- Gandhi, S., Kesseli, A., Zhang, Y., et al. 2023, *AJ*, 165, 242
- Gandhi, S. & Madhusudhan, N. 2019, *MNRAS*, 485, 5817
- García Muñoz, A. & Schneider, P. C. 2019, *ApJ*, 884, L43
- GharibNezhad, E., Shayesteh, A., & Bernath, P. F. 2013, *MNRAS*, 432, 2043
- Gibson, N. P., Nugroho, S. K., Lothringer, J., Maguire, C., & Sing, D. K. 2022, *MNRAS*, 512, 4618
- Guo, B., Yan, F., Nortmann, L., et al. 2024, *A&A*, 687, A103
- Herman, M. K., de Mooij, E. J. W., Nugroho, S. K., Gibson, N. P., & Jayawardhana, R. 2022, *AJ*, 163, 248
- Hoeijmakers, H. J., Kitzmann, D., Morris, B. M., et al. 2024, *A&A*, 685, A139
- Hooton, M. J., Hoyer, S., Kitzmann, D., et al. 2022, *A&A*, 658, A75
- Huang, C., Koskinen, T., Lavvas, P., & Fossati, L. 2023, *ApJ*, 951, 123
- Ilyin, I. V. 2000, PhD thesis, University of Oulu, Division of Astronomy
- Ishizuka, M., Kawahara, H., Nugroho, S. K., et al. 2021, *AJ*, 161, 153
- Johnson, M. C., Wang, J., Asnodkar, A. P., et al. 2023, *AJ*, 165, 157
- Keles, E., Czesla, S., Poppenhaeger, K., et al. 2024, *MNRAS*, 530, 4826
- Keles, E., Mallonn, M., Kitzmann, D., et al. 2022, *MNRAS*, 513, 1544
- Khorshid, N., Min, M., Désert, J. M., Woitke, P., & Dominik, C. 2022, *A&A*, 667, A147
- Kitzmann, D., Heng, K., Rimmer, P. B., et al. 2018, *ApJ*, 863, 183
- Kurucz, R. L. 2018, in *Astronomical Society of the Pacific Conference Series*, Vol. 515, *Workshop on Astrophysical Opacities*, 47
- Langeveld, A. B., Deibert, E. K., Young, M. E., et al. 2025, *ApJ*, 981, L32
- Lendl, M., Csizmadia, S., Deline, A., et al. 2020, *A&A*, 643, A94
- Li, G., Harrison, J. J., Ram, R. S., Western, C. M., & Bernath, P. F. 2012, *J. Quant. Spectr. Rad. Transf.*, 113, 67
- Lodders, K. 2002, *ApJ*, 577, 974
- Lodders, K. 2003, *ApJ*, 591, 1220
- Lothringer, J. D., Barman, T., & Koskinen, T. 2018, *ApJ*, 866, 27
- Lothringer, J. D., Rustamkulov, Z., Sing, D. K., et al. 2021, *ApJ*, 914, 12
- Madhusudhan, N. 2012, *ApJ*, 758, 36
- Madhusudhan, N., Amin, M. A., & Kennedy, G. M. 2014, *ApJ*, 794, L12
- Madhusudhan, N., Bitsch, B., Johansen, A., & Eriksson, L. 2017, *MNRAS*, 469, 4102
- Malik, M., Grosheintz, L., Mendonça, J. M., et al. 2017, *AJ*, 153, 56
- McKemmish, L. K., Masseron, T., Hoeijmakers, H. J., et al. 2019, *MNRAS*, 488, 2836
- McKemmish, L. K., Yurchenko, S. N., & Tennyson, J. 2016, *MNRAS*, 463, 771
- Meziani, Y. J., Flagg, L., Turner, J. D., et al. 2025, *AJ*, 170, 290
- Mollière, P., Wardenier, J. P., van Boekel, R., et al. 2019, *A&A*, 627, A67
- Mraz, G., Darveau-Bernier, A., Boucher, A., et al. 2024, *ApJ*, 975, L42
- Nugroho, S. K., Gibson, N. P., de Mooij, E. J. W., et al. 2020, *ApJ*, 898, L31
- Nugroho, S. K., Kawahara, H., Gibson, N. P., et al. 2021, *ApJ*, 910, L9
- Öberg, K. I., Murray-Clay, R., & Bergin, E. A. 2011, *ApJ*, 743, L16
- Pakhomov, Y. V., Ryabchikova, T. A., & Piskunov, N. E. 2019, *Astronomy Reports*, 63, 1010
- Parmentier, V., Line, M. R., Bean, J. L., et al. 2018, *A&A*, 617, A110
- Patrascu, A. T., Yurchenko, S. N., & Tennyson, J. 2015, *MNRAS*, 449, 3613
- Pelletier, S., Benneke, B., Ali-Dib, M., et al. 2023, *Nature*, 619, 491
- Pelletier, S., Benneke, B., Chachan, Y., et al. 2025, *AJ*, 169, 10
- Pelletier, S., Benneke, B., Darveau-Bernier, A., et al. 2021, *AJ*, 162, 73
- Petz, S., Johnson, M. C., Asnodkar, A. P., et al. 2024, *MNRAS*, 527, 7079
- Pinhas, A. & Madhusudhan, N. 2017, *MNRAS*, 471, 4355
- Pino, L., Désert, J.-M., Brogi, M., et al. 2020, *ApJ*, 894, L27
- Prinath, B., Hoeijmakers, H. J., Kitzmann, D., et al. 2022, *Nature Astronomy*, 6, 449
- Quirrenbach, A., Amado, P. J., Caballero, J. A., et al. 2016, in *Society of Photo-Optical Instrumentation Engineers (SPIE) Conference Series*, Vol. 9908, *Ground-based and Airborne Instrumentation for Astronomy VI*, ed. C. J. Evans, L. Simard, & H. Takami, 990812
- Rivlin, T., Lodi, L., Yurchenko, S. N., Tennyson, J., & Le Roy, R. J. 2015, *MNRAS*, 451, 634
- Ryabchikova, T., Piskunov, N., Kurucz, R. L., et al. 2015, *Phys. Scr*, 90, 054005
- Sába, A., Tsiaras, A., Morvan, M., et al. 2022, *AJ*, 164, 2
- Scandariato, G., Borsa, F., Bonomo, A. S., et al. 2023, *A&A*, 674, A58
- Sing, D. K., Lavvas, P., Ballester, G. E., et al. 2019, *AJ*, 158, 91
- Smith, P. C. B., Sanchez, J. A., Line, M. R., et al. 2024, *AJ*, 168, 293
- Southworth, J. 2010, *MNRAS*, 408, 1689
- Stock, J. W., Kitzmann, D., & Patzer, A. B. C. 2022, *MNRAS*, 517, 4070
- Strassmeier, K. G., Ilyin, I., Järvinen, A., et al. 2015, *Astronomische Nachrichten*, 336, 324
- Strassmeier, K. G., Ilyin, I., & Steffen, M. 2018a, *A&A*, 612, A44
- Strassmeier, K. G., Ilyin, I., & Weber, M. 2018b, *A&A*, 612, A45
- Tamuz, O., Mazeh, T., & Zucker, S. 2005, *MNRAS*, 356, 1466
- von Essen, C., Mallonn, M., Welbanks, L., et al. 2019, *A&A*, 622, A71
- Wakeford, H. R., Visscher, C., Lewis, N. K., et al. 2017, *MNRAS*, 464, 4247
- Wardenier, J. P., Parmentier, V., Lee, E. K. H., & Line, M. R. 2025, *ApJ*, 986, 63
- Weiner Mansfield, M., Line, M. R., Wardenier, J. P., et al. 2024, *AJ*, 168, 14
- Yan, F., Casasayas-Barris, N., Molaverdikhani, K., et al. 2019, *A&A*, 632, A69
- Yan, F., Nortmann, L., Reiners, A., et al. 2023, *A&A*, 672, A107
- Yan, F., Pallé, E., Reiners, A., et al. 2022a, *A&A*, 661, L6
- Yan, F., Pallé, E., Reiners, A., et al. 2020, *A&A*, 640, L5
- Yan, F., Reiners, A., Pallé, E., et al. 2022b, *A&A*, 659, A7
- Yang, Y., Chen, G., Wang, S., & Yan, F. 2024a, *AJ*, 167, 36
- Yang, Y., Chen, G., Yan, F., Tan, X., & Ji, J. 2024b, *ApJ*, 971, L8
- Yousefi, M., Bernath, P. F., Hodges, J., & Masseron, T. 2018, *Journal of Quantitative Spectroscopy and Radiative Transfer*, 217, 416
- Yurchenko, S. N., Williams, H., Leyland, P. C., Lodi, L., & Tennyson, J. 2018, *MNRAS*, 479, 1401
- Zechmeister, M., Anglada-Escudé, G., & Reiners, A. 2014, *A&A*, 561, A59
- Zhou, G., Huang, C. X., Bakos, G. Á., et al. 2019, *AJ*, 158, 141

Appendix A: Additional tables and figures

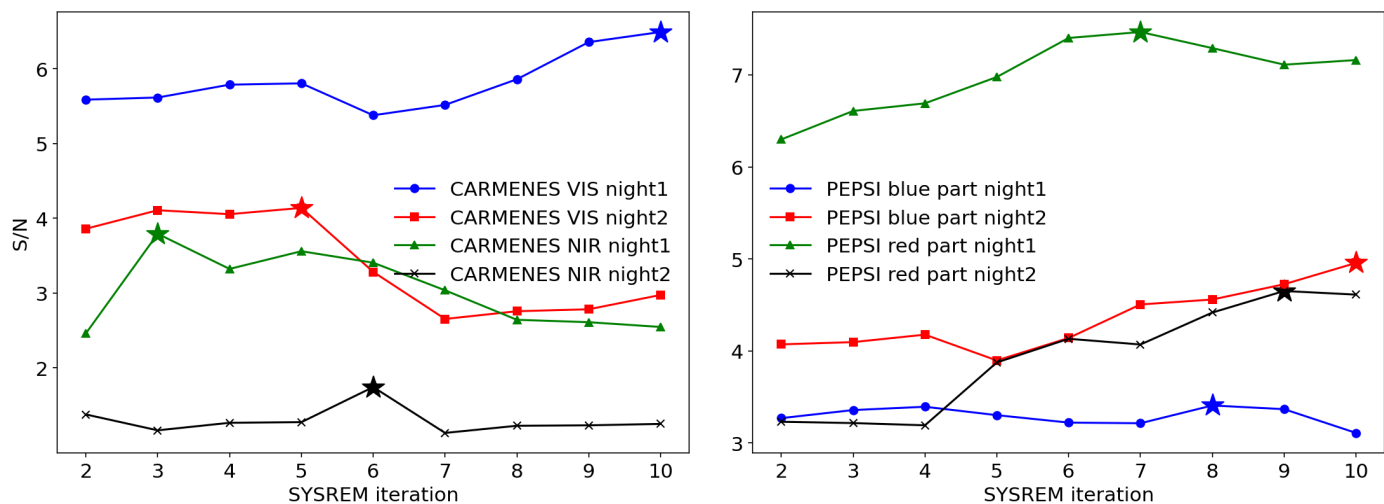


Fig. A.1: S/N values of the Fe I signal as a function of the SYSREM iteration. The highest S/N values are marked with stars. Each S/N value is measured at the peak position corresponding to the strongest detection signal.

Table A.1: Opacity databases employed for CCF calculation and atmospheric retrieval.

Chemical species	Opacity	References
Al I, Ba I, Ba II, Cl I, Ca I, Ca II, Cr I, Cr II, Fe I, Fe II, Li I, Mg I, Mg II, Na I, Ni I, Si I, Ti I, Ti II, Y I	Kurucz	Kurucz (2018)
Co I, Co II, Mn I, Sc I, Sc II, V I, V II	VALD	Pakhomov et al. (2019) ; Ryabchikova et al. (2015)
CaH, CrH, FeH, MgH, OH	MOLLIST	Bernath (2020) ; Li et al. (2012) ; GharibNezhad et al. (2013) ; Burrows et al. (2002) ; Yousefi et al. (2018) ; Brooke et al. (2016)
K I	Allard	Mollière et al. (2019)
AlH	AlHambra	Yurchenko et al. (2018)
AlO	ExoMol	Patrascu et al. (2015)
NaH	Rivlin	Rivlin et al. (2015)
TiO	Toto	McKemmish et al. (2019)
VO	VOMYT	McKemmish et al. (2016)

Notes. Opacity data for AlH, Ba I, Ba II, Co I, Co II, Cr I, CrH, Mn I, NaH, Ni I, Sc I, Sc II, V I, and V II were downloaded from the [DACE](#), while the remaining species were obtained via [petitRADTRANS opacity database](#).

Table A.2: Summary of the retrieved elemental abundances.

Element	FR: log(VMR)	FR: [X/H]	FR: [X/Fe]	ER: [X/H]	ER: [X/Fe]	$T_{\text{cond},50\%}$ (K)
C	< -3.09	< 0.56	< 0.28	< 0.74	< 0.50	40
Na	$-7.42^{+1.93}_{-4.84}$	$-1.64^{+1.93}_{-4.84}$	$-1.65^{+1.60}_{-5.09}$	$0.03^{+1.42}_{-1.81}$	$-0.07^{+1.24}_{-1.90}$	958
Mn	$-7.36^{+1.65}_{-4.02}$	$-0.78^{+1.65}_{-4.02}$	$-0.76^{+1.19}_{-4.33}$	$0.19^{+0.65}_{-1.21}$	$0.15^{+0.65}_{-1.01}$	1158
Cr	$-5.97^{+0.92}_{-1.32}$	$0.41^{+0.92}_{-1.32}$	$0.09^{+0.39}_{-0.53}$	$0.56^{+1.17}_{-1.02}$	$0.41^{+0.40}_{-0.46}$	1296
Fe	$-4.16^{+0.74}_{-1.11}$	$0.38^{+0.74}_{-1.11}$	0	$0.23^{+1.08}_{-0.98}$	0	1334
	$-2.50^{+1.12}_{-1.23}$ (Fe II)					
Mg	$-3.88^{+1.34}_{-1.05}$	$0.57^{+1.34}_{-1.05}$	$0.28^{+1.11}_{-0.74}$	$0.46^{+1.19}_{-1.22}$	$0.25^{+0.59}_{-0.63}$	1336
Ni	$-5.20^{+0.91}_{-1.22}$	$0.60^{+0.91}_{-1.22}$	$0.34^{+0.40}_{-0.58}$	$1.18^{+1.13}_{-1.02}$	$1.01^{+0.50}_{-0.60}$	1353
V	< -9.69	< -1.59	< -1.80	< 0.52	< -0.67	1429
Ca	$-9.66^{+2.11}_{-3.59}$	$-3.96^{+2.11}_{-3.59}$	$-3.91^{+1.73}_{-3.80}$	$-1.39^{+1.48}_{-1.07}$	$-1.37^{+0.98}_{-1.07}$	1517
	$-1.75^{+0.95}_{-2.07}$ (Ca II)					
Ti	$-8.36^{+0.96}_{-1.17}$	$-1.33^{+0.96}_{-1.17}$	$-1.51^{+0.56}_{-0.74}$	$-0.73^{+1.08}_{-0.91}$	$-0.85^{+0.55}_{-0.63}$	1582
Al	$-5.85^{+1.15}_{-1.88}$	$-0.28^{+1.15}_{-1.88}$	$-0.44^{+0.71}_{-1.56}$	$-0.04^{+1.19}_{-1.07}$	$-0.08^{+0.66}_{-0.94}$	1653
	$-7.00^{+1.51}_{-4.37}$ (Al I)					
	$-7.09^{+2.24}_{-5.08}$ (AlH)					

Notes. FR and ER denote the chemical free and chemical equilibrium retrieval, respectively. Except for aluminum, whose abundance was determined using both Al I and AlH, the abundances of all other elements were derived exclusively from their atomic species.

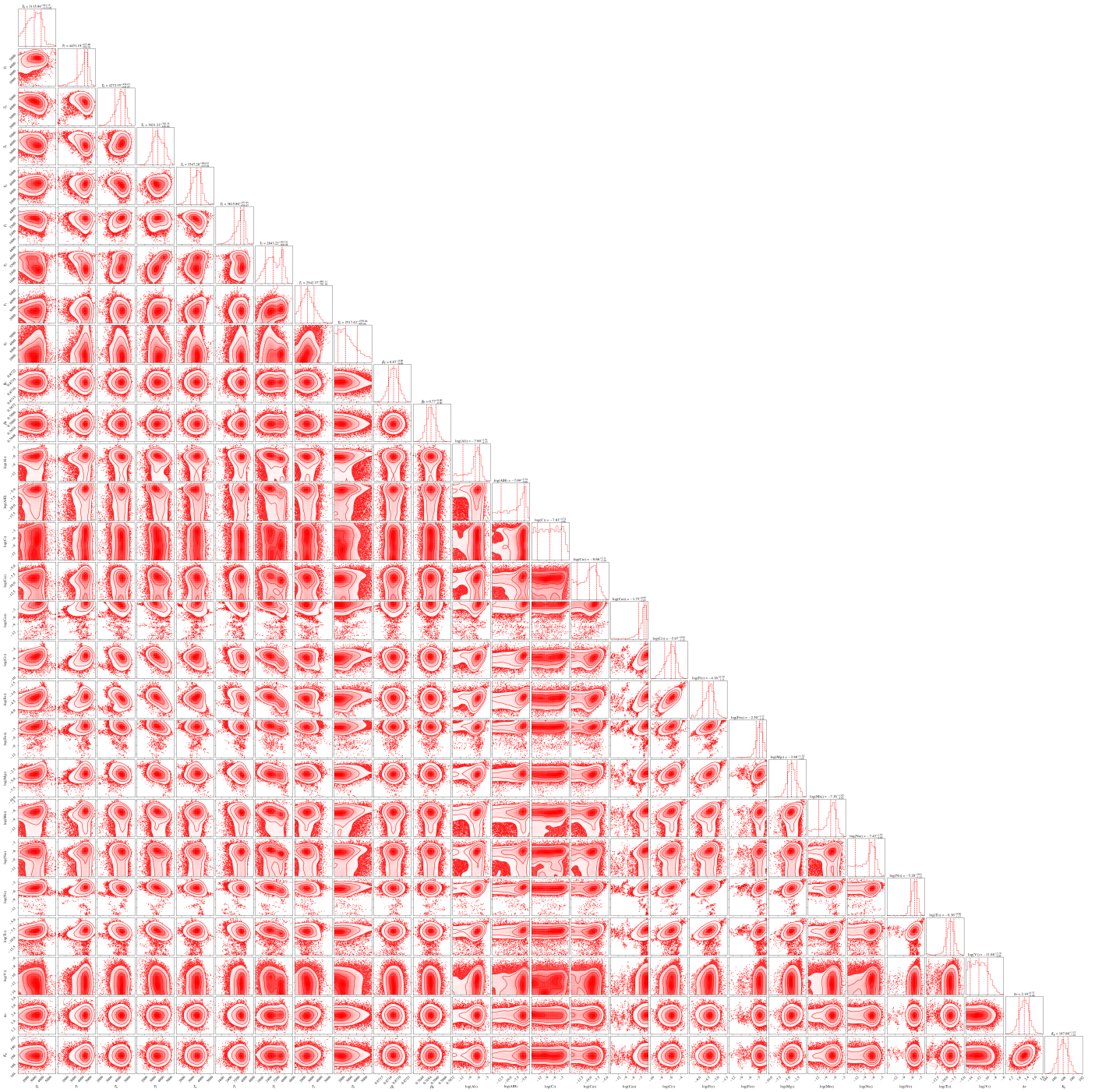


Fig. A.2: Posterior distribution of the parameters from the chemical free retrieval.

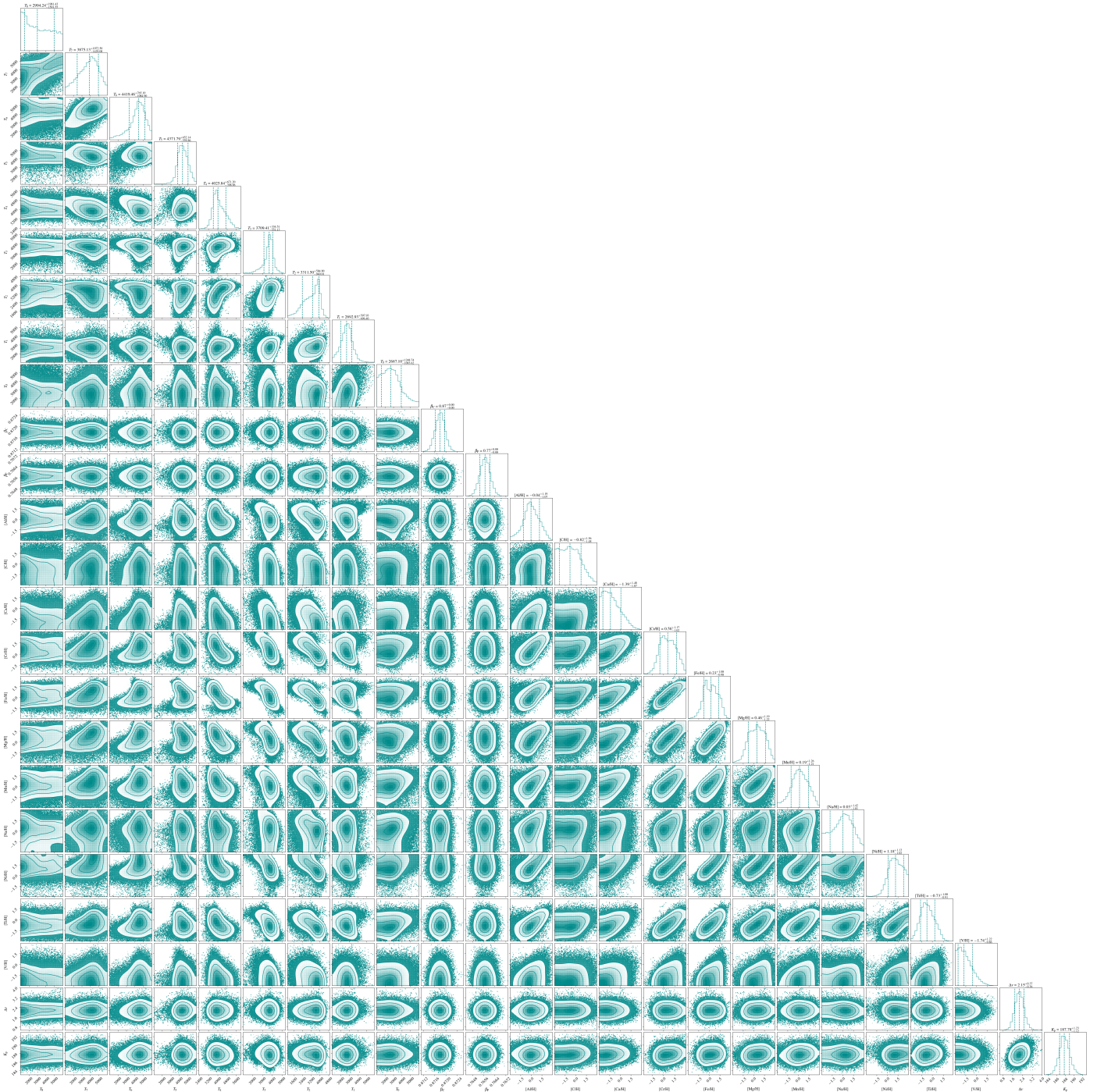


Fig. A.3: Posterior distribution of the parameters from the chemical equilibrium retrieval.